Arc-parallel flow within the mantle wedge: Evidence from the accreted Talkeetna arc, south central Alaska

Luc Mehl and Bradley R. Hacker
Department of Geological Sciences, University of California, Santa Barbara, California, USA

Greg Hirth and Peter B. Kelemen
Department of Geology and Geophysics, Woods Hole Oceanographic Institution, Woods Hole, Massachusetts, USA

Received 4 October 2002; revised 14 March 2003; accepted 2 April 2003; published 13 August 2003.

[1] Residual mantle exposures in the accreted Talkeetna arc, Alaska, provide the first rock analog for the arc-parallel flow that is inferred from seismic anisotropy at several modern arcs. The peridotites exposed at the base of the Jurassic Talkeetna arc have a Moho-parallel foliation and indicate dislocation creep of olivine at temperatures of $\sim$1000° to >1100°C. Slip occurred chiefly on the (001)[100] slip system, which has only rarely been observed to be the dominant slip system in olivine. Stretching lineations and olivine [100] slip directions are subparallel to the long axis of the Talkeetna arc for over 200 km, indicating that mantle flow was parallel to the arc axis. The alignment of the olivine [100] axes yields a calculated *S* wave anisotropy with the fast polarization direction parallel to the arc. Thus (1) the fast polarization directions observed parallel to some modern arcs now have an exposed geological analog; (2) arc-parallel fast polarization directions can be caused by anisotropic peridotites and do not require the presence of fracture zones, fluid-filled pockets, or glide on the (010)[001] H_2O-induced slip system; (3) seismic anisotropy beneath modern arcs may be due to slip on (001)[100] with a horizontal foliation rather than slip on (010)[100] with a vertical foliation; and (4) the observed dominance of the (001)[100] slip system may be due to high H_2O concentrations, suggesting that strain in the oceanic upper mantle may be accommodated dominantly by (001)[100] olivine slip. *INDEX TERMS:* 3902 Mineral Physics: Creep and deformation; 7218 Seismology: Lithosphere and upper mantle; 7230 Seismology: Seismicity and seismotectonics; 8120 Tectonophysics: Dynamics of lithosphere and mantle—general; 8123 Tectonophysics: Dynamics, seismotectonics; *KEYWORDS:* seismic anisotropy, upper mantle, lattice preferred orientation, olivine, peridotite, Talkeetna arc

Citation: Mehl, L., B. R. Hacker, G. Hirth, and P. B. Kelemen, Arc-parallel flow within the mantle wedge: Evidence from the accreted Talkeetna arc, south central Alaska, *J. Geophys. Res.*, *108*(B8), 2375, doi:10.1029/2002JB002233, 2003.

1. Introduction

[2] Regardless of driving force, plate tectonic theory suggests that plate motions are generally parallel to flow in the upper mantle. Theoretical models, experimental models, studies of ophiolites, and most measurements of upper mantle seismic anisotropy support this notion. In contrast, seismic anisotropy measured at many intraoceanic arcs indicates that mantle flow may be parallel to the arc and perpendicular to plate motion [*Wiens and Smith*, 2003]. The interpretation of arc-parallel flow from seismic anisotropy is based on the assumption that the measured anisotropy is due to the alignment of seismically fast olivine [100] axes with the flow direction. This assumption has recently been questioned by researchers hoping to confirm the more intuitive hypothesis that mantle flow is parallel to plate motion [e.g., *Jung and Karato*, 2001].

0148-0227/03/2002JB002233$09.00

[3] The accreted Talkeetna arc, south central Alaska, exposes a complete Jurassic arc section from mantle tectonite through a sedimentary carapace and thus provides invaluable insight into our understanding of subarc mantle flow. We have conducted a detailed metamorphic and structural petrology study of the mantle and gabbroic section of the Talkeetna arc to assess the relationships between mantle deformation and seismic anisotropy in this former intraoceanic arc. We document textural evidence that mantle flow was indeed parallel to the strike of the arc. Peridotite samples exhibit lattice preferred orientations (LPO) indicative of activation of the (001)[100], (010)[100], and {0kl}[100] slip systems and preferential alignment of the olivine fast [100] axes parallel to the arc. The alignment of [100] axes parallel to the strike of the arc is the same as predicted from seismic anisotropy measurements at several active arcs and provides the first field evidence for arc-parallel flow within the upper mantle. These observations suggest that 3-D flow needs to be included in the interpretation of

seismic data and future studies of subduction-zone dynamics.

2. Seismic Anisotropy, Dislocation Creep, and Lattice Preferred Orientations

[4] Since *Hess* [1964] first suggested the use of seismic anisotropy as a probe into the uppermost mantle the technique has expanded significantly, providing considerable new insight into geodynamics. Shear wave splitting, a manifestation of polarization anisotropy, refers to the splitting of a shear wave into orthogonal fast and slow components upon passage through an anisotropic medium [e.g., *Silver*, 1996]. Shear wave splitting within the mantle is believed to be due to propagation through strained peridotite [see reviews by *Silver*, 1996; *Savage*, 1999], such that the orientation of the observed splitting can be used to infer the kinematics of mantle flow [*Zhang and Karato*, 1995; *Savage*, 1999].

[5] The link between seismic anisotropy and the geologic record is the LPO of strained rocks. LPOs develop during dislocation creep, which is the dominant high-temperature deformation mechanism at elevated stresses or large grain sizes. The LPO that develops depends on the active slip system (slip plane and slip direction). During dislocation creep, the pole of the active slip plane rotates toward the shortening direction and the slip direction rotates toward the extension direction. LPOs are measured by recording the orientations of crystals with, for example, a universal stage or electron backscatter diffraction detector (EBSD).

[6] Shear wave velocities are influenced by lattice spacing, and because the lattice spacing for olivine is shortest in the [100] direction, the fast shear wave is polarized parallel to the greatest concentrations of olivine [100] axes for most propagation directions. Conveniently, deformation at mantle conditions usually aligns the [100] axes subparallel to the stretching, or flow, direction. The dominant slip system in 95% of the naturally deformed peridotites that have been studied is {0kl}[100] [*Ben Ismaïl and Mainprice*, 1998], which produces slip in the [100] direction on any of the {0kl} planes. Experimental studies show that at high shear strains ($\gamma \geq \sim 1$), the orientation of the [100] axes is controlled by the flow direction [*Zhang and Karato*, 1995]. Therefore at high strains the fast *S* wave polarization plane should be subparallel to the flow direction. In regions dominated by simple shear and lacking a tectonically complex lithosphere, such as at fast spreading ridges and above subducting slabs, the [100] maxima, the fast polarization plane, and the flow direction, are all predicted to be subparallel to the absolute plate motion [*McKenzie*, 1979; *Ribe*, 1989].

[7] Parts of this three-part prediction have been verified. Olivine LPOs with [100] maxima orthogonal to sheeted dikes have been observed in ophiolites such as in Oman [*Ceuleneer et al.*, 1988]. In addition, the fast *S* wave polarization plane has been recorded parallel to absolute plate motion at the East Pacific Rise [*Wolfe and Solomon*, 1998] beneath parts of eastern North America [*Barruol et al.*, 1997; *Fouch et al.*, 2000], in the Tonga back-arc [*Fischer and Wiens*, 1996; *Fischer et al.*, 2000], and in the Mariana [*Fouch and Fischer*, 1998] and Izu–Bonin subduction zones [*Fouch and Fischer*, 1996; *Hiramatsu and Ando*, 1996]. However, this simple picture is not universal. In continental settings, the fast polarization directions are often parallel to mountain belts [*Nicolas*, 1993] and major shear systems [Canadian Cordillera, *Bostock and Cassidy*, 1995; Pyrenees, *Barruol et al.*, 1998], probably reflecting frozen or active deformation in the lithosphere. However, several oceanic settings, presumably without fossilized structures, also show fast polarization planes oblique to plate motion [*Wiens and Smith*, 2003]. Fast *S* wave polarization planes have been observed subparallel to the Aleutian [*Yang et al.*, 1995], Hikurangi [*Gledhill and Stuart*, 1996], and central Honshu trenches [*Fouch and Fischer*, 1996], and to shear systems in the southern Kuril back arc [*Fouch and Fischer*, 1996], and beneath the Andean trench [*Russo and Silver*, 1994]. Observations of significant spatial variations in seismic anisotropy orientations add further complexity. For example, the fast *S* wave plane rotates from arc normal at the Fiji plateau to arc parallel approaching the Lau basin and Tonga trench [*Smith et al.*, 2001].

[8] There are several ways to explain why the fast polarization plane is not everywhere parallel to the assumed upper mantle flow direction in subduction zones. (1) Upper mantle flow may be more complicated than typically envisioned, and not everywhere parallel to absolute plate motion. (2) The assumption about which slip system is responsible for the anisotropy may be wrong. For example, *Jung and Karato* [2001] argued that H_2O-induced (010)[001] slip in olivine may align the fast seismic component perpendicular to the flow direction in hydrous (e.g., subduction-zone) environments. (3) Anisotropy may result from factors other than LPO, such as melt/fluid-filled cracks [*Kendall*, 1994] or other inhomogeneities within the volume sampled by the seismic wave [*Silver*, 1996]. We test these possibilities by measuring the LPOs from peridotites of the accreted Talkeetna arc of Alaska.

3. Talkeetna Arc

[9] The Talkeetna arc was active from 200 Ma to at least 180 Ma, and accreted to North America by the Late Jurassic or Early Cretaceous [*Burns*, 1985; *Plafker et al.*, 1989; *Rioux et al.*, 2001]. It is overlain to the north by Middle Jurassic conglomerate and bounded to the south by the Border Ranges Fault System (BRF), which has been interpreted as the megathrust or backstop during accretion [*Pavlis*, 1982; *Plafker et al.*, 1989]. We make the critical, but reasonable, assumption that the long axis of the active arc was parallel to its current orientation because discontinuous along-strike exposures of Talkeetna Formation volcanics and ultramafic bodies extend for ~1000 km (Figure 1a).

[10] The arc comprises a faulted, but otherwise complete, section of volcaniclastic rocks, hypabyssal and plutonic rocks, and mantle peridotite [*Barker and Grantz*, 1986; *Burns*, 1985; *Debari and Coleman*, 1989; *Plafker et al.*, 1989]. Thermobarometry from garnet gabbros and garnet gabbronorites from the base of the crust indicates equilibration at 1.1 GPa and 1025°C [*Kelemen et al.*, 2003], conditions perhaps typical of a 30-km-thick mature intraoceanic arc.

[11] The five peridotite exposures along the BRF (Figure 1a) have been described by *Burns* [1985] and *Debari and Coleman* [1989] and are only briefly summarized here. The southernmost exposures, predominantly cumulate dunite on

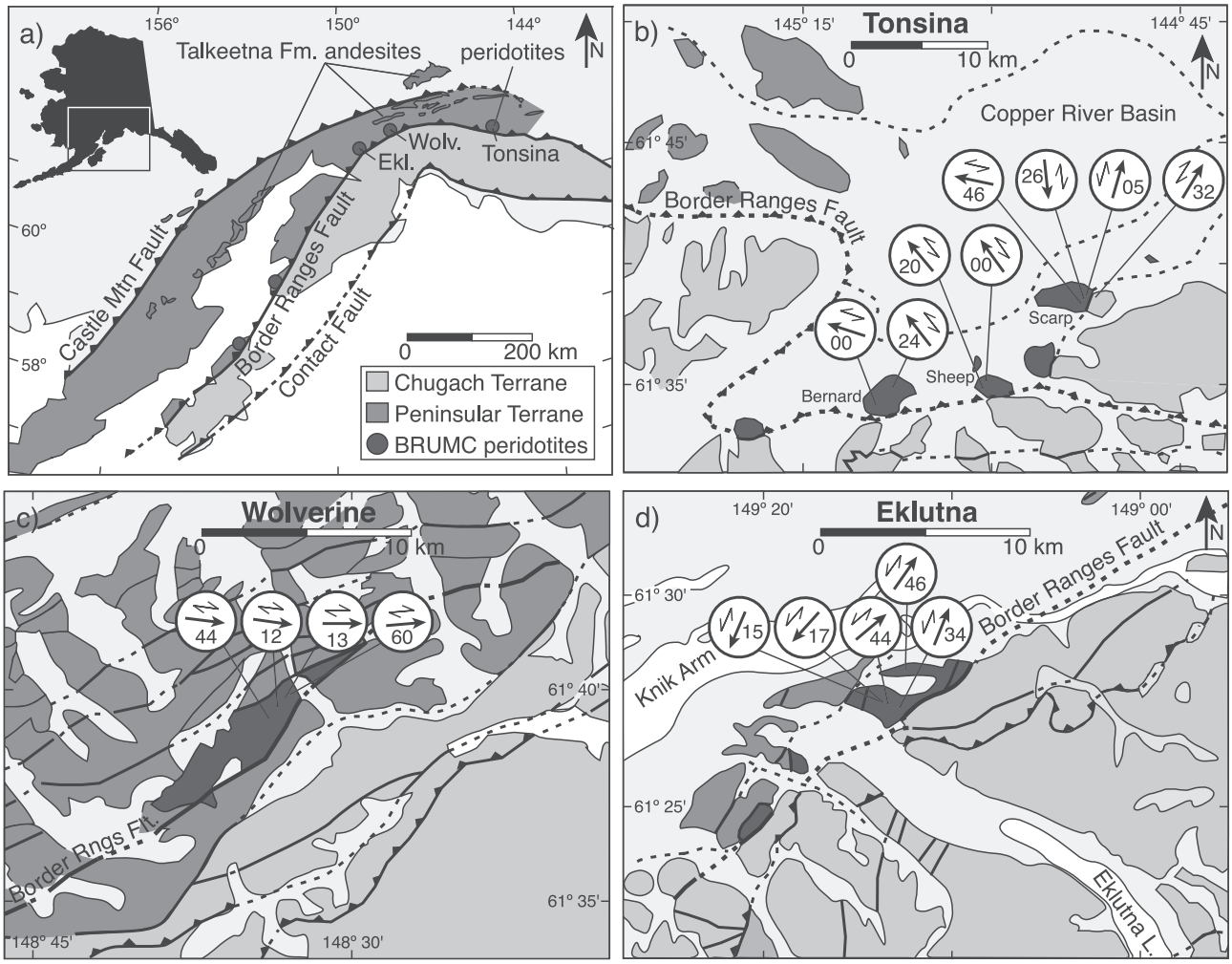

Figure 1. (a) Terrane map of south central Alaska. The Talkeetna arc is defined by ~1000 km of discontinuous Border Ranges Ultramafic-Mafic Complex (BRUMC) and Talkeetna Formation volcanic exposures. The structurally intact peridotites are (b) the residual tectonites of the Tonsina Complex and the cumulate dunites of the (c) Wolverine and (d) Eklutna Complexes. Black arrows and numbers indicate trend and plunge of lineations defined by elongate olivine, orthopyroxene, and spinel crystals. Sense of shear, as determined by LPO, is provided for each sample. Maps are modified from the work of *Millholland et al.* [1987] and *Debari and Coleman* [1989] (Figure 1a); *Winkler et al.* [1981] (Figure 1b); and *Winkler* [1992] (Figures 1c and 1d).

Kodiak Island and the Kenai Peninsula, are fault bounded within the subduction complex and do not help constrain flow geometry. The next two bodies to the north, the Eklutna and Wolverine Complexes, are >600 m thick cumulate sequences (lower crustal rocks) that extend ~11–12 km along the BRF and progress from chromite-bearing dunite up to websterite and gabbro. The easternmost peridotite body, the Tonsina Complex, is interpreted as residual mantle tectonite based on the presence of plastically deformed spinel and orthopyroxene and the absence of significant clinopyroxene. Of the four Tonsina peaks, Bernard Mountain (Figures 1b and 2) is the best exposed and is the focus of this and prior studies [e.g., *Debari and Coleman*, 1989]. The Tonsina Complex is underlain by the BRF to the south and overlain by cumulate websterite and gabbro to the north.

[12] The high-temperature fabrics at the base of the Talkeetna arc are most likely related to asthenospheric flow and not to emplacement or lithospheric processes. This interpretation is derived from the evidence that deformation occurred at high temperatures. Briefly, this evidence includes: (1) olivine slip systems indicate deformation above 1000°C; (2) thermobarometry from the base of the arc indicates that residual harzburgite fabrics predate the cooling of the crust below 1025°C; (3) interstitial orthopyroxenes in the harzburgite are blebby and have essentially random orientations, possibly indicating postdeformational crystallization at hyper-solidus temperatures; and (4) quartz fabrics (see Figures 1b and 7) indicate that the BRF may have had only a low-temperature, greenschist-facies history.

4. Results

4.1. Structure

[13] Bernard Mountain exposes a complete section from cumulate gabbro through residual peridotite, including ~250 m of garnet-bearing gabbro, norite, and gabbronorite,

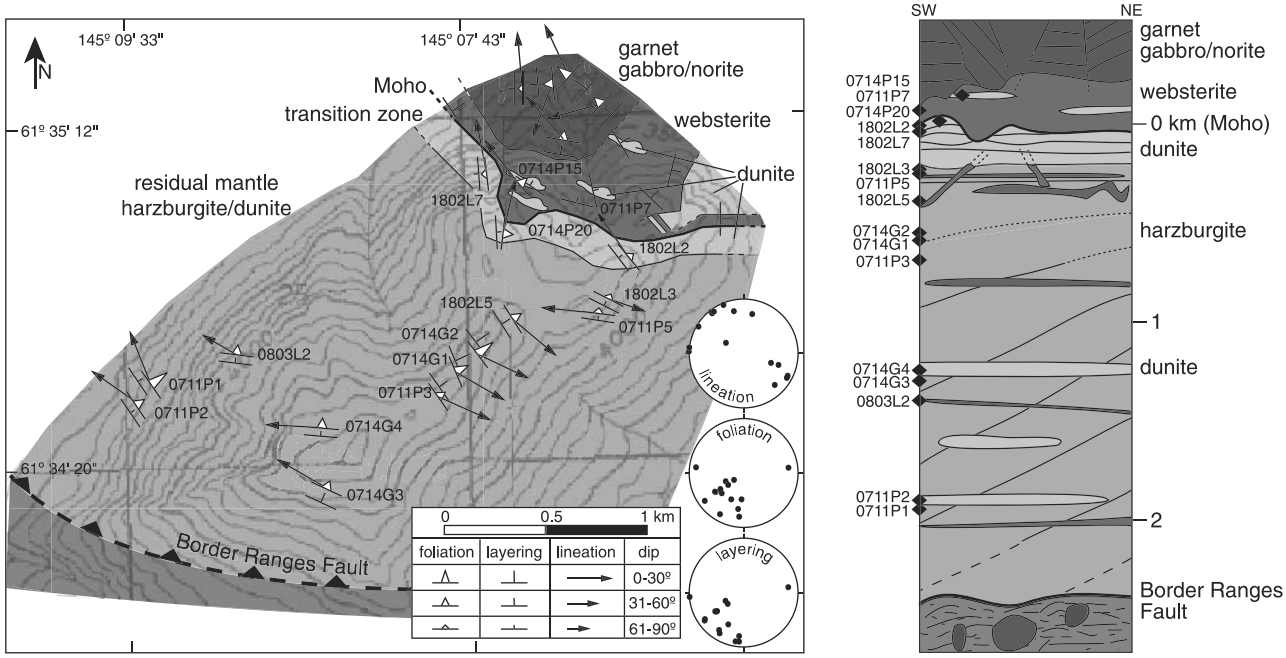

Figure 2. Bernard Mountain (see Figure 1 for location) geologic map, stereoplots of structural data for transect samples, and lithologic column. Foliation defined by the SPO of olivines, layering defined by spinel or orthopyroxene-rich layers. Thin lines in the restored column represent foliation, with spacing roughly proportional to strain. Column is perpendicular to lineation.

50–200 m of websterite, a ~100-m-thick transition zone of coarse chromite-bearing dunite, and ~2500 m of residual spinel harzburgite with interlayered dunite (Figure 2). The base of the cumulate websterite unit marks the petrologic Moho (transition from residual to cumulate rocks) and is a cataclastic layer several meters thick. Several observations indicate that displacement on the Moho-parallel fault that produced the cataclasite was limited. They are (1) the cataclasite is almost entirely websterite and does not incorporate harzburgite or gabbroic clasts; (2) the abundance of clinopyroxenite dikes increases toward the Moho websterites; and (3) a residual dunite lens within websterite and above the cataclastic layer has the same foliation, lineation, and olivine LPO as harzburgites beneath the Moho (0714P15 in Figure 4).

[14] The harzburgite section of Bernard appears to be structurally intact because layering, indicated by spinel-rich horizons and pyroxene-rich layers/dikes, dips consistently ~55°NNE. The layering is deformed in a few zones by open folds (~10 m wavelengths) or minor faults. Within the transition zone dunite the layering is often subvertical, perhaps as a result of folding. Thin clinopyroxenite dikes are common throughout the section and generally thicken from a few centimeters at the base of the section to a few meters near the Moho. Dikes near the Moho also have more variable orientations and commonly cut layering.

[15] Foliation in the peridotites is difficult to see, but generally parallels the compositional layering. The foliation is best defined in the field by flattened orthopyroxene or spinel-rich bands. Spinel aspect ratios range from ≤5:3:1 to 2:1:1. The shape-preferred orientation (SPO) of olivine grains was determined in thin section, and found to parallel the compositional layering for most of the Bernard section, although the SPO dips ~30° more steeply than the compositional layering at the base of the section (Figure 2). In several samples the foliation is weak.

[16] It was difficult to document the orientation of the lineation in the field. We routinely determined the orientation of lineations in the lab by cutting samples parallel to the compositional layering and then measuring the long axis of spinel or orthopyroxene grains under a binocular microscope. The samples were then reoriented and the lineation was recorded. There is some uncertainty in these calculations given the process of reorientation and also the presence of magnetite in many of the samples. However, we are confident of the measurements because the lineation is generally parallel between nearby samples and the olivine LPOs have [100] concentrations on or close to the primitive (see below).

4.2. Mineralogy and Textures

[17] Websterites above the petrologic Moho have cumulate textures and are composed of clinopyroxene (Di_{90-93}; all compositions determined by electron microprobe), 10–90% orthopyroxene (En_{86-87}), 0–30% olivine (Fo_{85-86}), and ~1% spinel that is usually located along pyroxene and olivine grain boundaries. The clinopyroxene is generally coarser than the orthopyroxene, and both range from ~0.5 to 6 mm. All the pyroxene grains are equidimensional, have weak to moderate undulatory extinction, exsolution lamellae, and straight to gently curved grain boundaries that show minimal evidence of grain-boundary migration.

[18] The ~100 m of dunite beneath the petrologic Moho (samples 0714P15 and 0714P20 in Figure 3) is texturally similar to dunites observed in the crust-mantle transition zones of ophiolites [e.g., *Nicolas and Prinzhofer*, 1983].

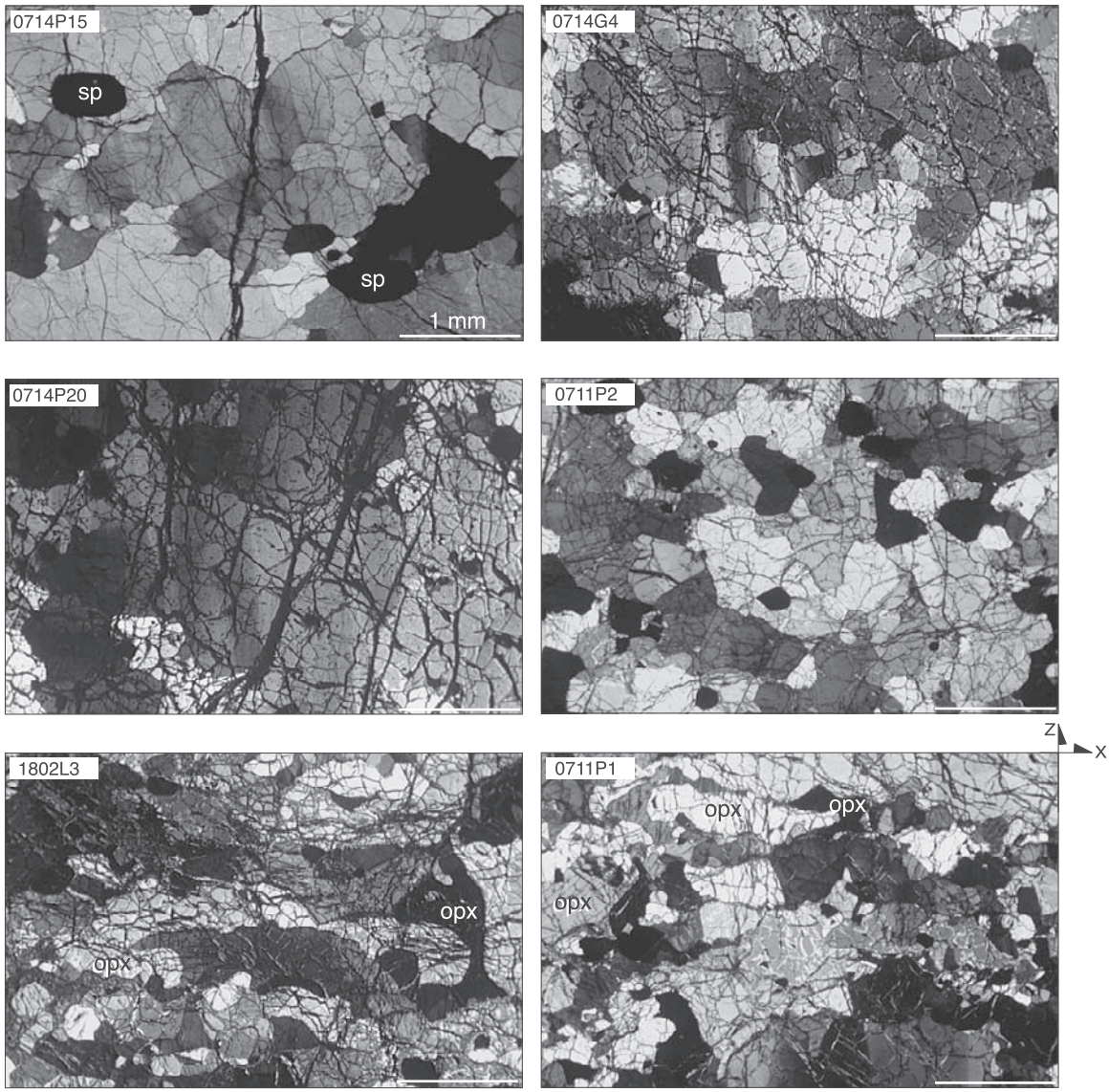

Figure 3. XPL photomicrographs of the XZ plane of Bernard Mountain residual tectonites. Scale bar in all photos is 1 mm. See Figure 2 for sample locations. Sample 0714P15 is from a dunite lens within the websterite unit and shows subparallel kink bands, serrate grain boundaries, and elongate spinels. Sample 0714P20 is a coarse dunite from the transition zone just beneath the Moho. Sample 1802L3 is a harzburgite from beneath the transition zone; note plastically deformed orthopyroxene and olivine. Samples 0714G4 and 0711P2 are dunites from lower in the section. Sample 0711P1 is a harzburgite from the base of the section.

Textures within the transition zone are highly variable, with both equidimensional and elongate grains (reaching aspect ratios of 8:1), and grain sizes ranging from 0.5 to 20 mm. The larger grains have pervasive subparallel subgrain boundaries. Both coarse and fine grains have highly irregular boundaries that vary from straight to curved or serrate. Grains are extensively recrystallized and the distribution of smaller, equant neoblasts around larger grains suggests subgrain rotation recrystallization. There is no textural evidence of significant postdeformational grain growth.

[19] Harzburgites beneath the transition zone (samples 1802L3 and 0714G4 in Figure 3) have high-temperature porphyroclastic textures similar to those reported from the residual mantle sections of many ophiolites [e.g., *Mercier and Nicolas*, 1975]. Harzburgites are ~85% olivine (Fo_{90-92}), up to 15% orthopyroxene (En_{91-92}), up to 3% clinopyroxene (Di_{94-95}), and $\leq$3% spinel (more Al rich than in the transition zone, based on the red-brown color in thin section). Rare olivine and orthopyroxene porphyroclasts are commonly slightly elongate and up to 6 mm across. The matrix grains surrounding the porphyroclasts are both subequant (~0.5 mm in diameter) and elongate, reaching aspect ratios of 5:1. Grain boundaries range from straight to serrated. Most of the matrix orthopyroxene is blebby and appears pinned between olivine grains. The Bernard harzburgites show no dominance of textures implying subgrain rotation versus grain-boundary migration recrystallization.

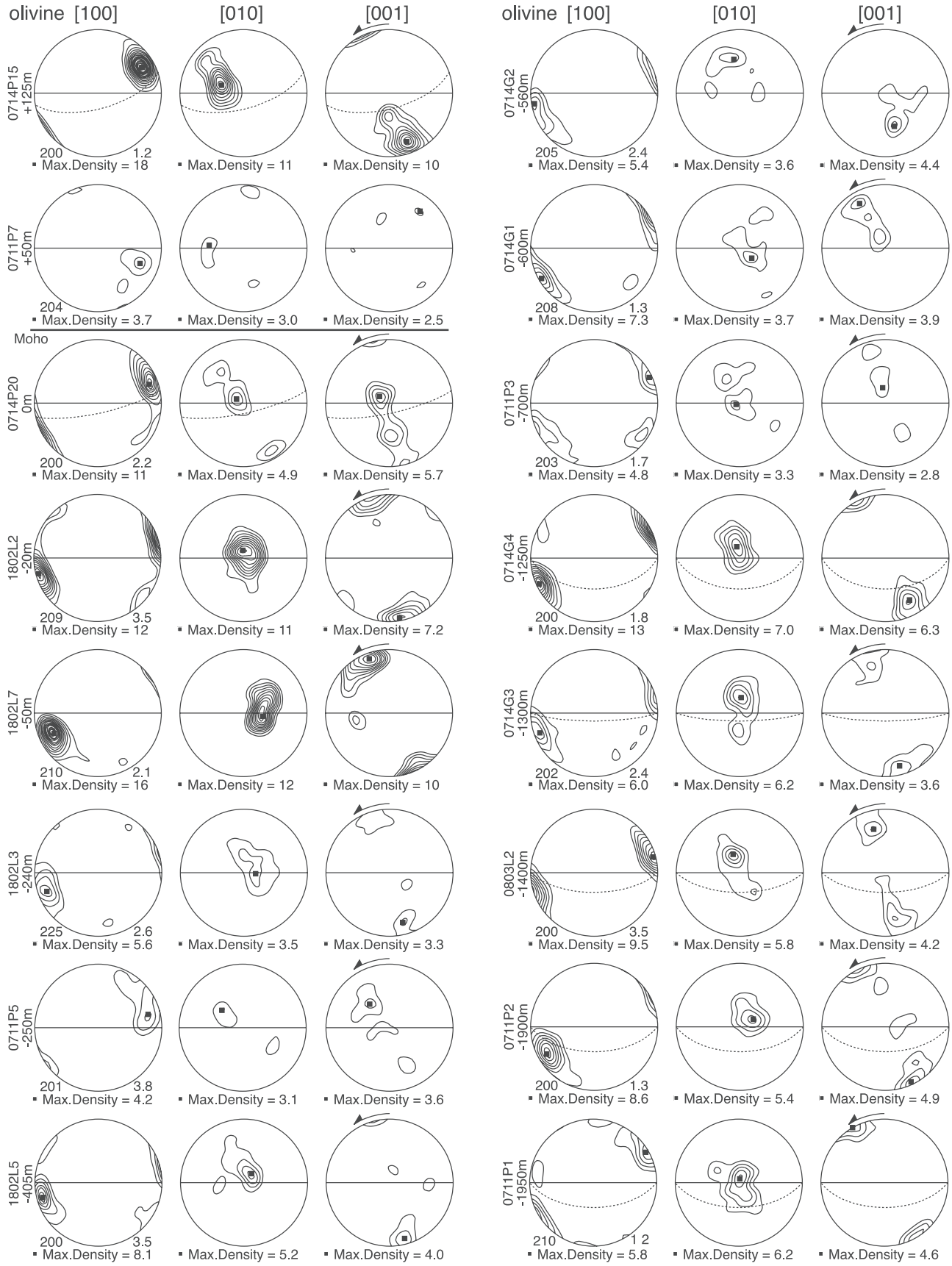
olivine [100]
[010]
[001]
0714P15 +125m
200 1.2
Max.Density = 18
Max.Density = 11
Max.Density = 10
0711P7 +50m
204
Max.Density = 3.7
Max.Density = 3.0
Max.Density = 2.5
Moho
0714P20 0m
200 2.2
Max.Density = 11
Max.Density = 4.9
Max.Density = 5.7
1802L2 -20m
209 3.5
Max.Density = 12
Max.Density = 11
Max.Density = 7.2
1802L7 -50m
210 2.1
Max.Density = 16
Max.Density = 12
Max.Density = 10
1802L3 -240m
225 2.6
Max.Density = 5.6
Max.Density = 3.5
Max.Density = 3.3
0711P5 -250m
201 3.8
Max.Density = 4.2
Max.Density = 3.1
Max.Density = 3.6
1802L5 -405m
200 3.5
Max.Density = 8.1
Max.Density = 5.2
Max.Density = 4.0
olivine [100]
[010]
[001]
0714G2 -560m
205 2.4
Max.Density = 5.4
Max.Density = 3.6
Max.Density = 4.4
0714G1 -600m
208 1.3
Max.Density = 7.3
Max.Density = 3.7
Max.Density = 3.9
0711P3 -700m
203 1.7
Max.Density = 4.8
Max.Density = 3.3
Max.Density = 2.8
0714G4 -1250m
200 1.8
Max.Density = 13
Max.Density = 7.0
Max.Density = 6.3
0714G3 -1300m
202 2.4
Max.Density = 6.0
Max.Density = 6.2
Max.Density = 3.6
0803L2 -1400m
200 3.5
Max.Density = 9.5
Max.Density = 5.8
Max.Density = 4.2
0711P2 -1900m
200 1.3
Max.Density = 8.6
Max.Density = 5.4
Max.Density = 4.9
0711P1 -1950m
210 1 2
Max.Density = 5.8
Max.Density = 6.2
Max.Density = 4.6

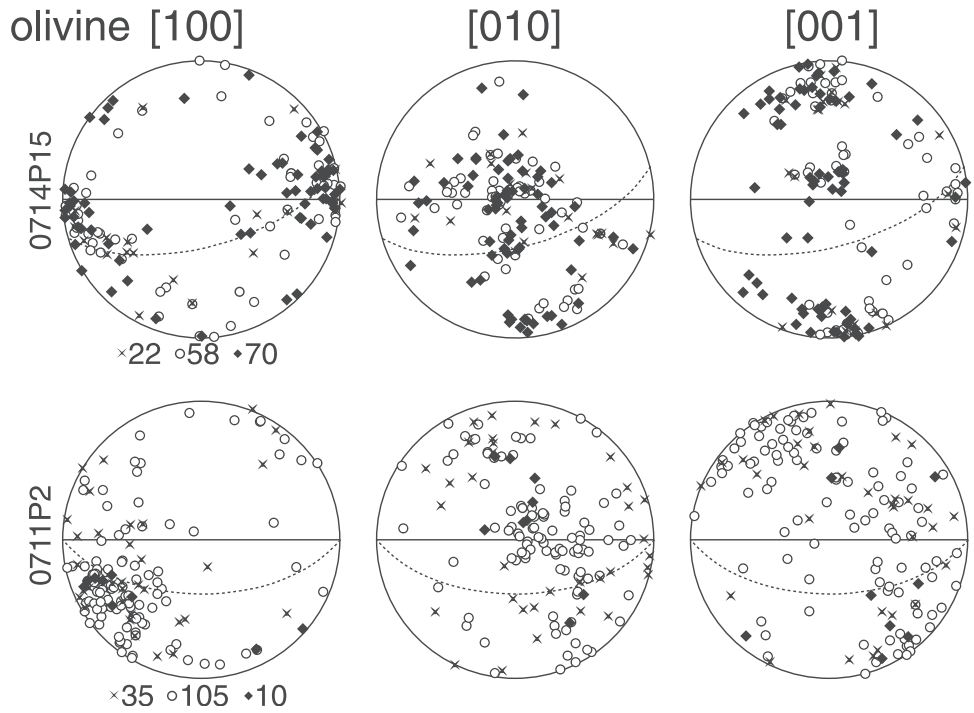

Figure 5. Olivine LPOs with respect to grain size. Plots follow the conventions of Figure 4. Symbols indicate <0.25 (crosses), 0.25–1 (open circles), and >1 mm (solid diamonds) divisions. The number of grains in each size division is listed at bottom. Orientations were measured with a universal stage optical microscope. There is an good agreement between LPOs measured by U-stage and EBSD (Figure 4) for these samples.

In addition, none of the samples have textures indicating significant postdeformational grain growth.

[20] Minor dunite bodies that crop out in the harzburgite section (e.g., sample 0711P2 in Figure 3) are texturally similar to the harzburgites, with ~0.5–2 mm elongate olivine grains with aspect ratios up to 4:1. Grain boundaries are mostly curved, and subgrain boundaries are more randomly oriented than in the transition zone dunites.

4.3. Lattice Preferred Orientations: Bernard Mountain

[21] A suite of 16 oriented samples was collected for petrofabric study along a vertical structural profile at Bernard Mountain. Thin sections were mechanically polished and given a 24-hour colloidal silica polish followed by washing with petroleum ether or citric acid to remove silica residue. The samples were sputter coated with Au-Pd and then most of the coating was rubbed off on paperboard. LPOs were measured at the University of California, Santa Barbara, CA with an HKL Technology electron backscatter diffraction detector (EBSD) and Channel 5 software on a JEOL 6300 scanning electron microscope operated at 15 kV and ~10 nA. At least 200 crystals with diffraction patterns that differed from their immediate neighbor were manually selected and analyzed in each sample; typically, this resulted in analysis of 10–15% area of each thin section. Five of these samples were also analyzed with a universal stage; good agreement was found between the two methods (compare Figures 4 and 5).

[22] LPO data from Bernard Mountain are shown in Figure 4 and Table 1. All the olivine fabrics show [100] maxima subparallel to the lineation, indicating dislocation glide in the [100] direction. [100] is the shortest Burgers vector for olivine and therefore the easiest slip direction [*Nicolas and Poirier*, 1976]. The concentration of [001] subparallel to the foliation pole suggests that the dominant slip plane for the Talkeetna samples is (001). The (001)[100] slip (i.e., slip on the 001 plane in the 100 direction) has been recognized as a high-temperature (>1000°C) slip system [e.g., *Carter and Avé Lallemant*, 1970; *Nicolas and Poirier*, 1976], but has only rarely been observed to dominate in naturally or experimentally deformed rocks (see Section 5). The weak [010] and [001] girdles in several samples is evidence for dislocation glide on the more common {0kl}[100] system, also recognized as a high-temperature,

Figure 4. (opposite) Pole figures for olivine [100], [010], and [001] axes for Bernard Mountain residual tectonites in equal-area, lower hemisphere projections. First contour is 2σ, contour interval is one multiple of random distribution (Kamb method). Foliation is indicated by the E-W line and lineation is at the intersection of the foliation and the primitive. Layering, when different from foliation (see text), is indicated by dashed line. Number of grains, shear strain, and maximum density are listed at lower left, lower right, and bottom of each plot, respectively. Sense of shear is determined by the orientation of the slip plane with respect to the foliation and is indicated. Samples are ordered from top to bottom of the section, sample height, next to sample number, refers to position relative to the Moho; see Figure 2 for locations.

Table 1. Structural and LPO Data[a]

Location	Sample	*Z*, m	Lith.	S_0	S_1	L	α	θ	γ	SOS	Slip System
Bernard	0714P15	+125	D	033, 72	048, 46	322, 08	26	30	1.2	S	(001)[100]
Bernard	0711P7	+50	O W	...	...	...	0	0	...	...	...
Bernard	0714P20	0	D	085, 90	097, 78	013, 27	12	21	2.2	S	{0kl}[100]
Bernard	1802L2	−20	H	054, 77	054, 77	325, 07	0	15	3.5	S	(001)[100] and (100)[001]
Bernard	1802L7	−50	H	264, 72	264, 72	347, 22	0	22	2.1	S	(001)[100]
Bernard	1802L3	−240	H	030, 76	030, 76	109, 32	0	19	2.6	S	(001)[100]
Bernard	0711P5	−250	H	006, 70	006, 70	276, 00	0	14	3.8	S	{0kl}[100]?
Bernard	1802L5	−405	H	056, 53	056, 53	136, 18	0	15	3.5	S	(001)[100]
Bernard	0714G2	−560	H	053, 30	053, 30	117, 08	0	20	2.4	S	(001)[100]
Bernard	0714G1	−600	H	065, 30	065, 30	120, 08	0	29	1.2	S	(001)[100]
Bernard	0711P3	−700	H	055, 52	055, 52	110, 45	0	25	1.7	S	{0kl}[100] and (100)[001]?
Bernard	0714G4	−1250	H	005, 80	005, 40	272, 00	40	24	1.8	S	(001)[100]
Bernard	0714G3	−1300	H	025, 55	025, 45	300, 05	10	20	2.4	S	(001)[100]
Bernard	0803L2	−1400	D	009, 81	009, 56	300, 60	25	15	3.5	S	(001)[100]
Bernard	0711P2	−1900	D	054, 50	054, 18	338, 05	32	29	1.2	S	(001)[100]
Bernard	0711P1	−1950	H	055, 76	055, 44	322, 05	32	30	1.2	S	(001)[100]
Bernard	Bulk	...	H	...	...	...	0	15	3.5	S	(001)[100]
Sheep	0713G4	...	D	305, 65	305, 65	320, 20	0	16	3.2	S	{0kl}[100]
Sheep	0713G1	...	H	054, 66	054, 66	324, 00	0	18	2.8	S	(010)[100]&{0kl}[100]
Sheep	0713P21	...	W	255, 75	255, 75	351, 68	0	40	0.4?	S?	cpx: (100)[001]
Scarp	1710L7	−150	H	231, 51	231, 51	174, 26	0	0–35	0.7+	Z	(010)[100]
Scarp	1710L9	−100	H	275, 50	275, 50	282, 46	0	0–35	0.7+	S	(001)[100] and (100)[001]?
Scarp	0712B1	...	Q	311, 78	311, 78	036, 32	0	12	4.5	Z	(c)<a>
Scarp	2711L10	...	Q	305, 35	305, 35	025, 08	0	10	5.5	Z	(c) and (r)<a>
Scarp	2711L9	...	Q	horiz.	horiz.	035, 00	0	10	5.5	S	(c)<a>
Scarp	2711L7	...	Q	333, 47	333, 47	060, 08	0	15	3.5	S	(c)<a>
Wolverine	2714L5	+580	D	155, 60	*155, 60*	098, 44	*0*	25	1.7	Z	(100)[001]
Wolverine	2714L3	+305	D	172, 37	172, 37	097, 12	*0*	16	3.2	Z	(100)[001]
Wolverine	2714L2	+60	D	162, 54	*162, 54*	090, 13	*0*	19	2.6	Z	{0kl}[100]
Wolverine	2714L1	0	D	144, 65	*144, 65*	085, 60	*0*	15	3.5	Z	{011}[100]
Wolverine	Bulk	...	D	...	...	...	*0*	10	5.5	Z	{0kl}[100]
Eklutna	2808L4	+430	D	119, 75	*119, 75*	022, 34	*0*	10	5.5	S	(001)[100]
Eklutna	2809L3	–	D	310, 87	*310, 87*	035, 46	*0*	5	11	S	{0kl}[100]
Eklutna	2808L6	+120	D	082, 51	*082, 51*	050, 44	*0*	5	11	S	{0kl}[100]
Eklutna	0708P1	+60	D	099, 49	147, 50	222, 17	35	25	1.7	S	{0kl}[100]
Eklutna	2808L1	+0	D	089, 55	*089, 55*	203, 15	*0*	12	4.5	S	{0kl}[100]
Eklutna	Bulk	...	D	...	...	...	*0*	10	5.5	S	{0kl}[100]

[a]Definitions are as follows: *Z*, position (meters) in relation to Moho (Bernard), or relative to lowermost sample (Wolverine and Eklutna); lith., lithology, D, dunite, H, harzburgite, W, websterite, O W, olivine websterite, Q, quartz; S_0, layering (dip direction, dip); S_1, foliation (dip direction, dip); *L*, lineation (dip direction, dip); α, angle between foliation and layering; θ, angle between foliation and slip plane; γ, minimum shear strain; SOS, sense of shear, S, sinistral, Z, dextral; italics indicate low confidence or assumed.

~1000°C, slip system [*Carter and Avé Lallemant*, 1970]. Analysis of several samples with a universal stage revealed no clear change in LPO as a function of grain size, indicating that the same slip system(s) were active during the deformation of all grains (Figure 5).

[23] To further document that deformation was dominated by slip on (001)[100], we measured crystal orientations across several low-angle subgrain boundaries, or tiltwalls. Because tiltwalls are formed of edge dislocations, the orientation of the tiltwall and the lattice rotation across the tiltwall can be used to evaluate the dominant slip system. As shown in Figure 6, [100] tiltwalls within crystals from the Bernard samples show rotation about the [010] axis, indicating that the walls are formed predominantly by edge dislocations from the (001)[100] system. Other crystals show rotation consistent with activity of the (100)[001] and (010)[100] systems.

[24] In all samples the inferred orientation of the dominant slip plane is oblique to the foliation, indicating a simple shear deformation history [*Nicolas et al.*, 1973; *Bouchez et al.*, 1983]. All samples indicate sinistral shear, which may have implications for the tectonic history of the arc. In addition, the [001] and [010] concentrations are typically half as strong as the [100] maximum, suggesting activation of the (010)[100] or {0kl}[100] slip systems, a component of constrictional strain, or perhaps transtension [e.g., *Tommasi et al.*, 1999].

[25] To compare samples within the section, we calculated shear strains from the angle between the foliation and the fabric. Calculated shear strains range from 0.7 to 3.8 (Figure 4 and Table 1), although these values could be minima if the grain-shape foliation is a steady state foliation modified by recrystallization [e.g., *Means*, 1981; *Lister and Snoke*, 1984], or maxima if the LPO is not parallel to the shear direction, such as observed in experimental samples at shear strains less than ~1 [*Zhang and Karato*, 1995]. There is a weak inverse correlation between apparent strain and the strength of the fabric: several samples with low shear strains have very strong LPO (0714P15, 0714G4), whereas samples indicating greater shear have significantly weaker fabrics (1802L3, 1802L5). The cause of this trend is unclear, but may be due to one of the processes mentioned above (the strong LPO representing a steady state foliation or the weak LPO not yet parallel with the shear direction). In addition, the strain at which the LPO becomes parallel to the shear direction may change

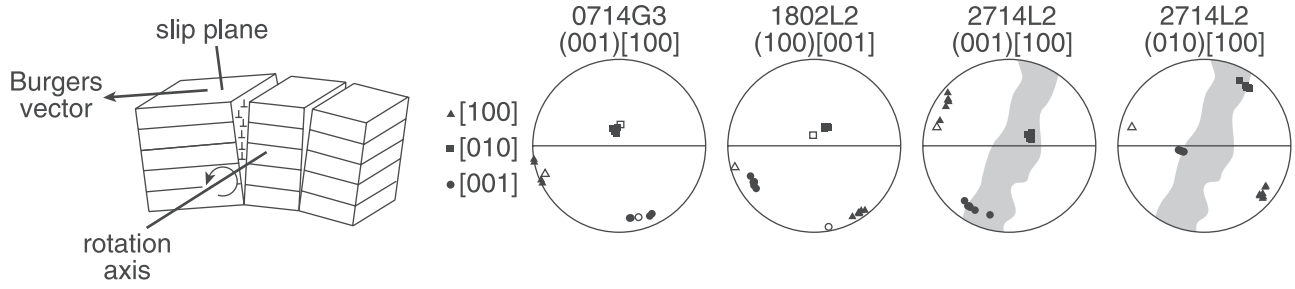

Figure 6. Lattice rotation and tiltwall orientations across single olivine crystals. Stereoplots follow the conventions of Figure 4 and show orientations of several points within each crystal, as determined by EBSD. The rotation axis is indicated by the olivine axis that varies the least. The remaining two olivine axes are interpreted as the slip plane and Burgers vector, which can be distinguished by their orientation relative to the lineation. Olivine [100], [010], and [001] axes are indicated by triangles, squares, and circles, respectively. Open symbols indicate maximum concentration orientations for the corresponding whole rock LPO ($\geq$200 crystals). Sample 0714G3 shows evidence for slip on (001)[100], while 1802L2 indicates slip on the conjugate (100)[001] system (see also 1802L2 in Figure 4). Sample 2714L2 deformed by slip on {0kl}[100] (indicated by the gray field of [010] and [001] axes), but slip on both (010)[100] and (001)[100] is indicated by the single-crystal analyses.

under different deformation conditions. In light of these uncertainties we emphasize that these calculations are solely for comparison of fabric-foliation obliquity between samples.

[26] Orthopyroxene and clinopyroxene LPOs are shown in Figure 8. The only clinopyroxene fabric is from a cumulate websterite above the Moho and is random. Orthopyroxene grains from the residual harzburgite are typically either large "porphyroclasts" (>1 mm) or small blebby crystals ($\sim$250 μm) pinned between olivine grains. Surprisingly, both types of grains have similar, essentially random, orientations. The weak to absent LPOs and blebby textures could be due to postdeformation crystallization. If so, this implies deformation at hyper-solidus ($\geq$1100°C) temperatures.

4.4. Lattice Preferred Orientations: Neighboring Tonsina Peaks

[27] The olivine LPOs from Sheep Mountain harzburgites (refer to Figure 1b for location) show high-temperature fabrics similar to those measured from Bernard Mountain (Figure 7 and Table 1). Sheep Mountain is mostly composed of harzburgite and a websterite unit with many dunite lenses at various orientations. The olivine LPOs from these lenses have the same strength, similar slip systems, obliquity between foliation and LPO, and NW-SE lineations as the Bernard section. Although most of the websterites at Bernard Mountain have random LPOs (see 0711P7 in Figures 4 and 7), one olivine websterite from Sheep Mountain shows a strong clinopyroxene LPO (sample 0713P21 in Figure 8). This sample has a high foliation-fabric obliquity and an LPO perhaps suggesting activation of the high-temperature (100)[001] slip system [*Avé Lallemant*, 1978].

[28] Scarp Mountain to the NE is more complex. The peridotite section at Scarp Mountain is composed of coarse chromite-bearing dunites similar to the transition-zone dunites at Bernard Mountain. Lineation trends are not uniform (Figure 1b) and the olivine LPOs consist of two [100] maxima and partial girdle [010] or [001] concentrations, perhaps implying a change in kinematics or an influence of dynamic recrystallization [*Lee et al.*, 2002]. Fabrics dominated by slip on both (001)[100] and (010)[100] are observed (Figure 7).

4.5. Fabrics: Wolverine and Eklutna Complexes

[29] To compare deformation fabrics along the arc, LPOs were measured on samples from the Wolverine and Eklutna Complexes (Figures 1c and 1d), $\sim$150 and 200 km west of Tonsina, respectively. These complexes have cumulate sequences that grade from chromite-bearing dunite to websterite and gabbronorite [*Burns*, 1985]. In general, the rocks have equigranular olivine (Fo_{85-87}) grains up to 6 mm across, up to 15% clinopyroxene (Di_{93-95}) (both intercumulous and matrix), rare orthopyroxene, and equant spinel both between and within matrix grains. Olivine grains have straight, curved, or serrate boundaries. Olivines in most samples have subparallel subgrain boundaries throughout, although olivines in several samples have only weak undulatory extinction. Because these rocks are coarse grained, it is difficult to see a SPO and thus the foliation plane was assumed to parallel the compositional layering. This assumption is supported by the few samples with well-defined SPO.

[30] Wolverine and Eklutna samples have strong LPOs that suggest slip on the {0kl}[100] systems, with either the (001), (010), or possibly (011) slip planes dominant in different samples (Figures 9 and 10). Dunites and gabbros at Wolverine have a southeast-dipping foliation and an E-W trending lineation (Figure 1c). The lineation could not be identified for samples 2714L3 and 2714L5, but if it is assumed to be E-W like the other samples, the fabrics are indistinguishable from rocks lower in the section. The foliation is variable in the Eklutna Complex, but generally dips to the east. Lineations plunge shallowly NE and SW and all samples indicate sinistral shear (Figure 1d). All Wolverine samples indicate dextral shear, opposite to the Eklutna and Tonsina Complexes; the cause is unknown.

[31] The slip direction, mineral lineation, and inferred strike of the arc are subparallel in the Wolverine and Eklutna

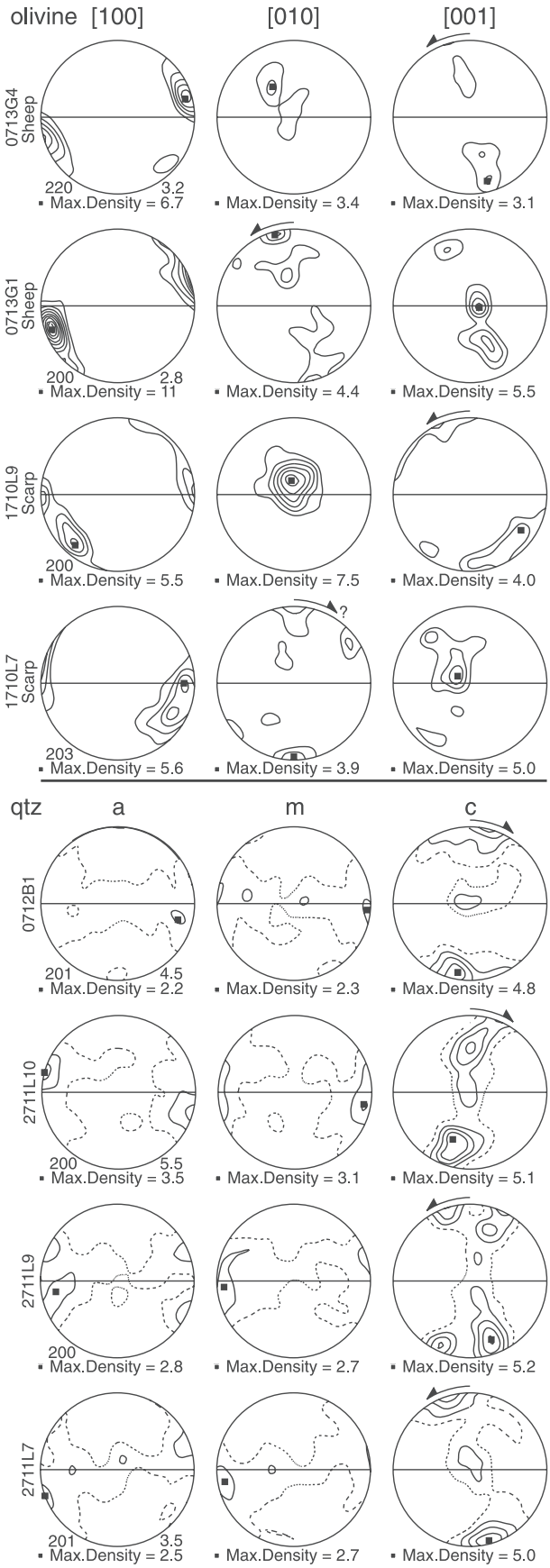

Figure 7. (opposite) Olivine and quartz lattice preferred orientations for Sheep and Scarp Mountain rocks, see Figure 4 for plot conventions; refer to Figure 1b for locations. Quartz samples are from a schist just east of the BRF at Scarp Mountain. The dashed contours are 1σ.

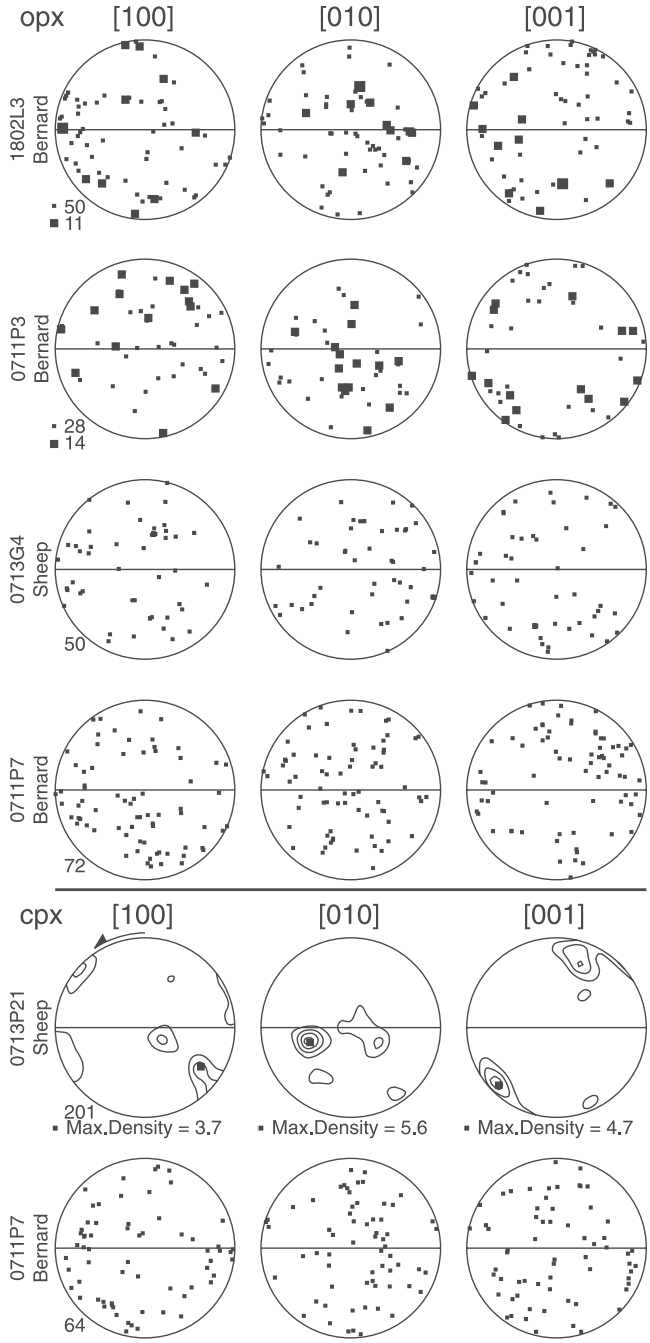

Figure 8. Pole figures for orthopyroxene [100], [010], and [001] axes and clinopyroxene [100], [010], and [001] axes for Tonsina samples. Plots follow the conventions of Figure 4. Large squares in 1802L3 and 0711P3 show orientation of ''porphyroclastic'' rather than blebby orthopyroxene. Fabrics are essentially random except 0713P21.

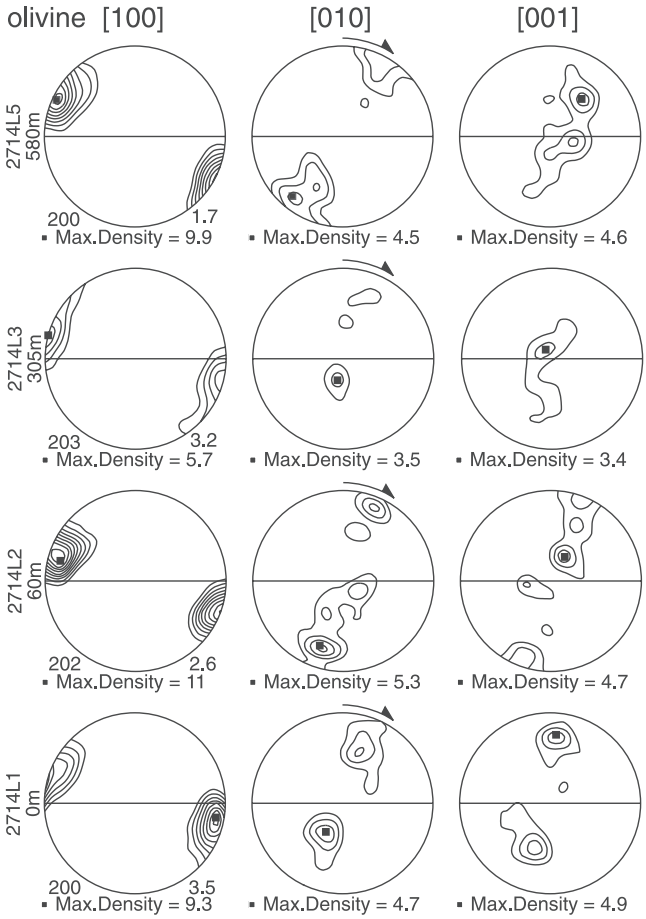

Figure 9. Olivine LPOs for the Wolverine Complex, see Figure 4 for plot conventions. Sample heights refer to position above the lowermost sample.

dunites, similar to the Tonsina samples. The fact that these cumulate bodies show the same strong LPO and high-temperature slip systems as the residual Tonsina Complex suggests that the mantle deformation extended into the crust.

4.6. Fabrics: Summary

[32] The Talkeetna arc peridotites indicate deformation at temperatures exceeding 1000°C. Dislocation creep of olivine in residual peridotite samples was dominated by the (001)[100] slip system, with additional slip along (010)[100] and {0kl}[100] in some samples. Pyroxenes comprise $\leq$15% of the harzburgites and are randomly oriented. Slip on {0kl}[100] dominates the samples from the cumulate Wolverine and Eklutna sections, and the slip vector, mineral lineation, and inferred strike of the arc are subparallel, as observed for the Tonsina Complex. Samples indicate sinistral shear at Tonsina (top-NW), dextral shear at Eklutna (top-east), and sinistral shear (top-SW) at Eklutna. Shear is along a Moho-parallel foliation, and most apparent shear strains range from 0.7 to 3.8. Thus the concentration of olivine [100] axes, which controls the seismic properties, is inclined 15°–35° from the mineral lineation. This inclination would be difficult to detect with *S* wave splitting because the axis of rotation would be subhorizontal in a restored section (horizontal Moho).

4.7. Seismic Anisotropy

[33] To compare seismic anisotropy at modern arcs to the Talkeetna rocks, we calculated seismic properties for residual Tonsina samples based on the mineral orientation data (LPO) and density, using the software of *Mainprice* [1990]. We calculated velocities at 1.0 GPa and 1000°C [minimum estimates for the Bernard mantle section, *Kelemen et al.*, 2003] using Voigt-Reuss-Hill averaging and single-crystal elastic constants and derivatives ($\partial C_{ij}/\partial T$ and $\partial C_{ij}/\partial P$) from experimental studies. Olivine coefficients are from the work of *Kumazawa and Anderson* [1969], and orthopyroxene coefficients are from that of *Kumazawa* [1969] and *Frisillo and Barsch* [1972]. Most Bernard samples did not have sufficient orthopyroxene orientation analyses to be representative of the volume fraction of orthopyroxene, so we

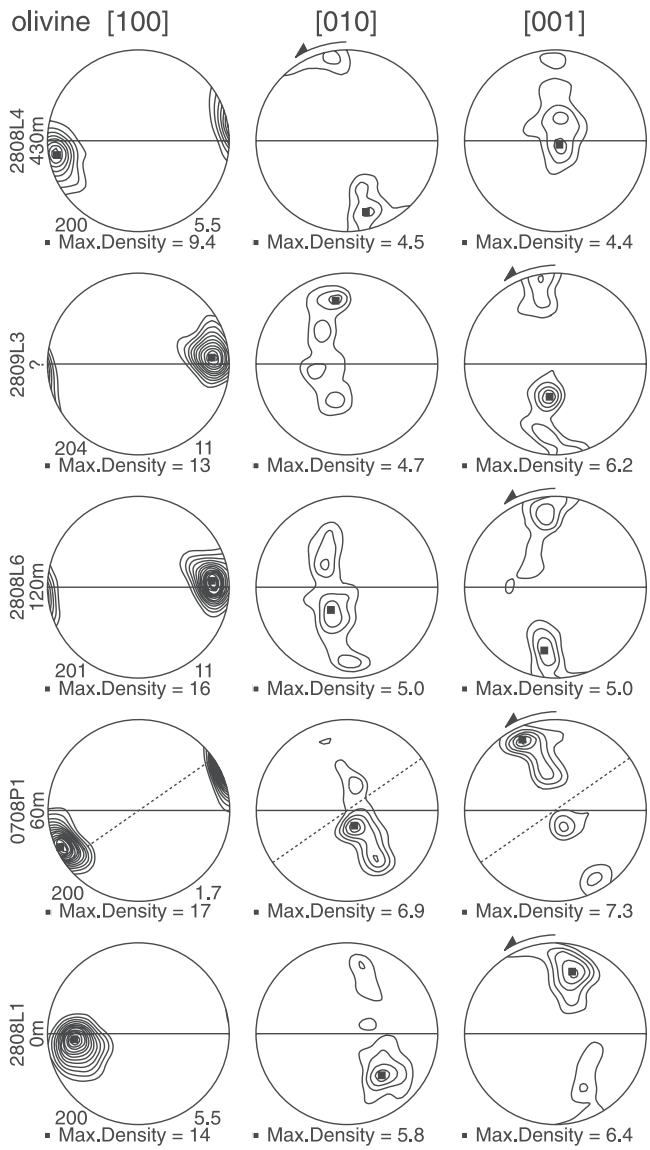

Figure 10. Olivine lattice preferred orientations for the Eklutna Complex, see Figure 4 for plot conventions. Heights refer to position above the lowermost sample.

applied the orientations from sample 1802L3 (50 grains) to all Bernard samples. The orthopyroxene data alone have a maximum anisotropy of 2–3%, but given the volume fraction (up to 15%), their inclusion lowered calculated anisotropies by ~10%. The geothermal gradient beneath the arc is high enough that the effect of temperature exceeds that of pressure and produces slower velocities at 1.0 GPa and 1000°C compared with STP.

[34] Calculated 3-D seismic properties for end-member Bernard samples are shown as lower hemisphere stereoplots in Figure 11 and Table 2. Because many seismic studies are limited to phases with incidence angles less than a critical angle of ~30°, our plots shade orientations outside this shear wave window. The maximum calculated anisotropy ranges from 6.4 to 17% and from 5.6 to 13% for *P* and *S* waves, respectively, similar to those calculated from other peridotites [e.g., *Ben Ismaïl and Mainprice*, 1998]. The calculated seismic properties consistently show that for most propagation directions the fast *S* wave polarization plane is parallel to the maximum concentration of olivine [100] axes, and subparallel to the long axis of the Talkeetna arc.

5. Discussion

5.1. Seismically Measured Anisotropies, Calculated Peridotite Anisotropies

[35] Because our calculated *S* wave anisotropies for individual samples are significantly greater than seismic measurements from mantle wedges (which generally range from 0.5 to 2% assuming coherent anisotropic layer thicknesses from 400 to 80 km, respectively, *Savage* [1999]), we calculate the integrated anisotropy of "bulk" Talkeetna samples (Figure 12 and Table 2). The bulk Bernard calculation is obtained by combining all 2873 measured crystal orientations in the 2-km-thick sampled section, using the petrologic Moho as the reference frame, and assuming that the section is composed of 85% olivine and 15% orthopyroxene (orthopyroxene orientations are from sample 1802L3, see above). The maximum *S* wave anisotropy calculated for the bulk section is 6.4%, weaker than the mean value of 8.8%. This anisotropy produces a maximum birefringence of 0.3 km/s. Thus, for shear waves traveling normal to the Moho, V_{S_1} = 4.58 km/s and V_{S_2} = 4.34 km/s resulting in a 0.024-s delay for *S* waves traveling through the 2-km-thick Bernard section. In other words, a Bernard-like section ~80 km thick would be sufficient to produce the 1-s splitting delay typical of observations at most subduction zones [*Savage*, 1999].

[36] Calculations for the Wolverine and Eklutna Complexes include elastic coefficients for clinopyroxene [*Levien et al.*, 1979; *Matsui and Busing*, 1984]; because the temperature derivatives for clinopyroxene elasticity are unknown we used the orthopyroxene derivatives from the work of *Frisillo and Barsch* [1972]. As with orthopyroxene, even though the clinopyroxene orientation data do not yield significant anisotropies (1.6–2.7% for the bulk Eklutna and Wolverine Complexes, respectively), their inclusion lowers the bulk anisotropy by ~14%. These cumulate peridotites produce slightly greater *S* wave anisotropy (~7%) and similar delay times (0.3 km/s) to the Bernard section (Figure 12 and Table 2).

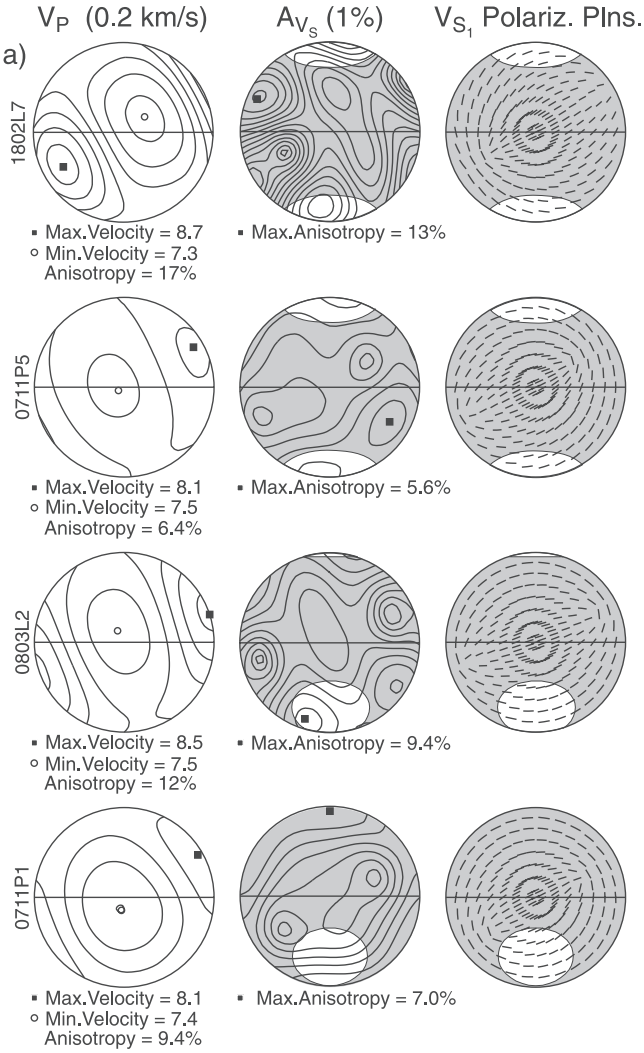

Figure 11. Estimated seismic properties at 1000°C and 1.0 GPa for representative Bernard Mountain residual harzburgites. See Figures 2 and 4 for Bernard sample locations and LPOs. Calculations use a Voigt-Reuss-Hill average of stiffness [*Mainprice*, 1990]. All plots are equal-area, lower hemisphere projections, foliation is indicated by the E-W line, and lineation is at the intersection of the foliation and primitive. Contour interval for *P* wave velocity is 0.2 km/s and for *S* wave anisotropy is 1%. The shaded regions indicate propagation directions outside of the shear wave window (see text) when the Moho is restored to horizontal. Refer to Table 2 for *P* and *S* wave velocities, anisotropy, and mineral proportions.

[37] It is apparent from Figure 12 that the magnitude of anisotropy of the bulk sections is controlled by the alignment of olivine [100] axes. The [010] and [001] concentrations are weak, due to the activity of multiple slip planes within the {0kl}[100] systems (refer to Figure 6), different shear strains of the samples, and possibly a varying constrictional strain component. The calculated anisotropy of the bulk Bernard section is significantly greater than that calculated from seismic measurements. Because [100] orientations are more consistent than [010] and [001] axes from sample to sample, it is unlikely that simply adding

Table 2. Calculated Seismic Properties at 1000°C and 1.0 GPa for Talkeetna Arc Peridotites[a]

Sample	% Ol	Position	V_P max	V_P min	A_{V_P}	V_{S_1} max	V_{S_1} min	V_{S_2} max	V_{S_2} min	A_{V_S} max	A_{V_S} min	d_{V_S} min
1802L7	100	top	8.72	7.33	17.3	4.89	4.42	4.49	4.19	13.26	0.49	0.61
0711P5	85	upper	8.05	7.54	6.4	4.63	4.43	4.51	4.34	5.56	0.11	0.25
0803L2	95	middle	8.45	7.48	12.2	4.75	4.44	4.52	4.26	9.42	0.20	0.43
0711P1	85	base	8.13	7.40	9.4	4.67	4.41	4.49	4.32	7.00	0.07	0.32
Bernard	85	bulk	8.16	7.48	8.8	4.66	4.45	4.50	4.32	6.43	0.27	0.29
Wolverine	90	bulk	8.38	7.57	10.2	4.64	4.47	4.49	4.24	7.14	0.11	0.32
Eklutna	96	bulk	8.37	7.58	9.8	4.67	4.48	4.52	4.25	6.95	0.44	0.31

[a]Definitions are as follows: % Ol, percent olivine in rocks. Calculations assume that the remainder is orthopyroxene for Bernard and clinopyroxene for Wolverine and Eklutna. Position, structural position in Bernard section when the Moho is restored to horizontal; V_P max, min, maximum and minimum velocities for *P* waves; A_{V_P} maximum *P* wave anisotropy; V_{S_1} max, min, maximum and minimum velocities for fast *S* waves; V_{S_2} max, min, maximum and minimum velocities for slow *S* waves; A_{V_S} max, min, percent anisotropy for *S* waves; d_{V_S} maximum time delay in seconds between fast and slow *S* waves. Elastic constants and PT derivatives are from the work of *Kumazawa and Anderson* [1969] for olivine, *Kumazawa* [1969], *Frisillo and Barsch* [1972] for orthopyroxene, and *Levien et al.* [1979] and *Matsui and Busing* [1984] for clinopyroxene.

more samples to the bulk calculations would lower the calculated anisotropy to match subduction-zone measurements. Alternatively, the mantle section sampled by seismic waves may contain olivine deformed by slip along directions other than [100], or more likely for asthenospheric conditions, the *S* waves may pass through peridotites with different flow directions at different depths [see modeling by *Buttles and Olson*, 1998], i.e., there may be complex flow within the mantle wedge.

[38] In all three bulk samples, the fast [100] axes are subparallel to the mineral lineation. Thus when the Talkeetna arc was active, the fast polarization plane would have been subparallel to the strike of the arc (Figure 13), consistent with seismic observations at modern arcs [e.g., *Smith et al.*, 2001; *Wiens and Smith*, 2003].

5.2. Can the (001)[100] Slip System be Induced by Elevated H_2O Activity?

[39] The (001)[100] slip system was dominant within the residual mantle beneath the Talkeetna arc, in contrast to observations of naturally and experimentally deformed peridotites, as well as consideration of the olivine crystal structure, which indicate that the easiest olivine slip system at high temperatures is (010)[100] [*Nicolas and Poirier*, 1976; *Zhang and Karato*, 1995; *Bystricky et al.*, 2000; *Zhang et al.*, 2000]. Numerical simulations using viscoplastic self-consistent theory and equilibrium-based models also produce dominant slip on (010)[100] even when (001)[100] is assigned an equal critical resolved shear stress, because strain compatibility requires activity of the (010)[001] system [*Tommasi et al.*, 2000]. Dominance of (001)[100] slip has only been generated by fabric modeling that incorporates dynamic recrystallization when the (100)[001] and (010)[001] slip systems are assigned equal critical resolved shear stresses [*Wenk and Tomé*, 1999].

[40] Given the tectonic setting of the Talkeetna arc and the likelihood that deformation took place in a wet, subduction-zone, environment, we suggest that the dominance of (001)[100] slip is a result of elevated H_2O activity. Experimental deformation of olivine at elevated H_2O conditions is limited, but supports a link between the (001)[100] system and H_2O. *Mackwell et al.* [1985] determined that olivine single crystals are weakest under wet conditions when compressed parallel to $[101]_c$; this orientation favors primary slip on (001)[100] and secondary slip on (100)[001] under dry conditions [*Durham and Goetze*, 1977]. Some of the LPOs from the Talkeetna arc suggest that (100)[001] may have been active (note the weak secondary [100] and [001] peaks in sample 1802L2 (Figures 4 and 6) and [100] peaks in samples 1802L5 and 0711P3 (Figure 4), such peaks could also be due to recrystallization; see *Lee et al.* [2002]).

[41] Experiments on olivine aggregates also indicate that crystals in the $[101]_c$ orientation are weakest at elevated H_2O contents and moderate stresses and that these crystals control the developing LPO [*Jung and Karato*, 2001]. However, the "type-C" fabrics that develop in Jung and Karato's experiments indicate that the (100)[001] system dominates over the conjugate (001)[100] system. The (001)[100] fabric in the Talkeetna samples suggests that the dominant Burgers vector switches from [001] at the relatively high stresses of Jung and Karato's experiments to [100] at lower stresses, such as experienced during deformation in the arc. A change in Burgers vector with decreasing stress suggests that the stress exponent for the (001)[100] system is lower than that for the (100)[001] system.

[42] To compare the Talkeetna samples with the experiments of Jung and Karato, we calculated the OH concentration, C_{OH}, for H_2O-saturated olivine corresponding to the minimum (cooling) PT estimates at the base of the arc. We used the relationship [*Zhao et al.*, 2003; see *Hirth and Kohlstedt*, 2003]:

$$C_{OH} = A_{H_2O} \exp[-(E_{H_2O} + PV_{H_2O})/RT] f_{H_2O},$$

where A_{H_2O} = 26 H/10^6 Si/MPa, E_{H_2O} = 40 kJ/mol, $V_{H_2O} = 10 \times 10^{-6}$ m^3/mol, f_{H_2O} = water fugacity in MPa. The OH concentration, C_{OH}, in saturated olivine ranges from 422 to 945 H/10^6 Si at pressures of 1–1.1 GPa, temperatures of 1000°–1200°C, and f_{H_2O} = 1826–1968 MPa [extrapolated from the work of *Tödheide*, 1972]. We emphasize that these are maximum values for H_2O content at these conditions, however, high H_2O contents are calculated for the source of some primitive arc magmas [e.g., *Baker et al.*, 1994]. Thus despite the fact that the Talkeetna arc mantle is residual, i.e., depleted, it might still have contained enough H_2O to fall within the field of *Jung and Karato* [2001] for H_2O-induced slip systems (see their Figure 2).

[43] Peridotites with LPOs indicating a dominance of (001)[100] slip, although rare, have been described from a number of locations. Two of these, dredge samples from the Tonga and Mariana arcs [*Nicolas et al.*, 1980], are from tectonic settings for which high H_2O contents could be

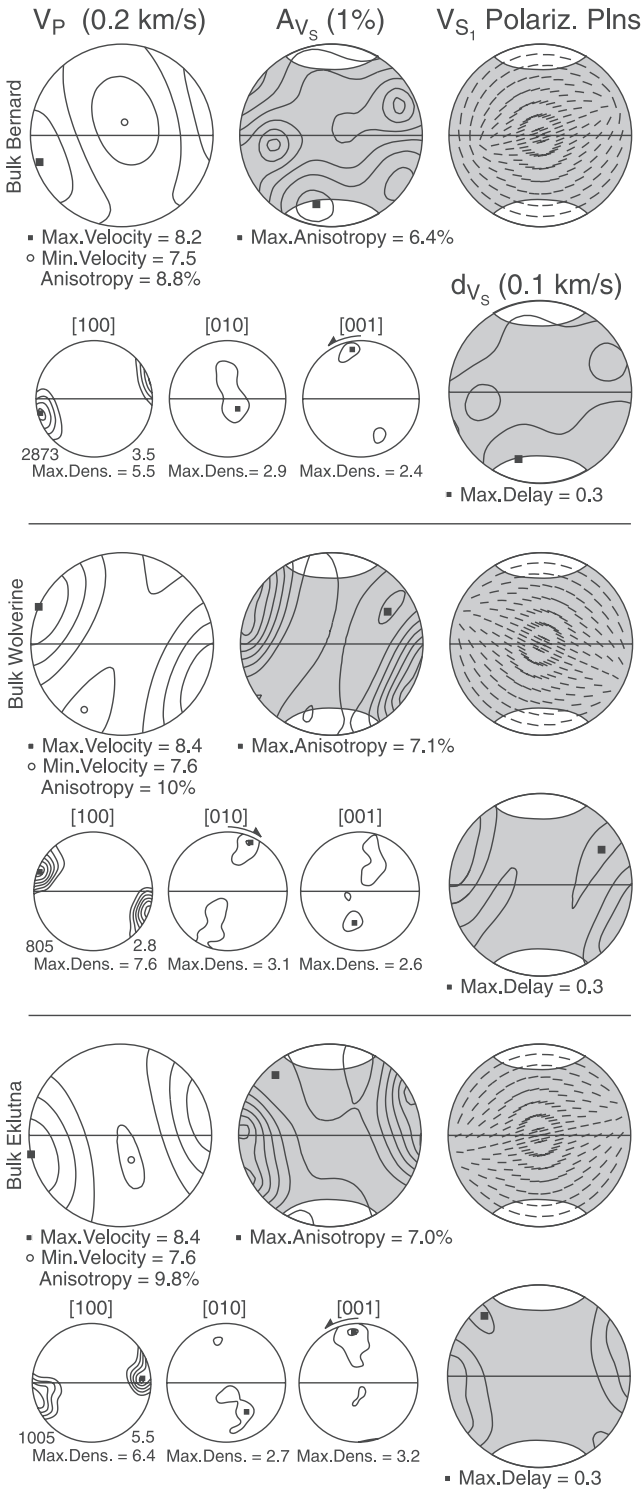

Figure 12. Estimated seismic properties and olivine LPO for bulk Bernard Mountain, Wolverine and Eklutna Complexes at 1000°C and 1.0 GPa. See Figures 4 and 11 for plot conventions. Mineral proportions are as follows: Bernard: 85% olivine, 15% orthopyroxene; Wolverine: 90% olivine, 10% clinopyroxene; Eklutna: 94% olivine, 6% clinopyroxene.

expected. However, in other cases, a clear link to deformation at high H_2O contents is not established [e.g., the Voltri Massif, NW Italy, *Van Der Wal et al.*, 1992; the Bay of Islands Ophiolite, *Mercier*, 1985; *Suhr*, 1993; New Caledonia, the Betic Cordillera, and the Erro-Tobbio massif, *Tommasi et al.*, 2000].

[44] It is generally assumed that the common high-temperature (010)[100] fabrics from the mantle section of ophiolites, such as in Oman, represent asthenospheric deformation [*Nicolas et al.*, 1980; *Nicolas and Violette*, 1982; *Rabinowicz et al.*, 1984; *Ceuleneer et al.*, 1988]. However, conditions beneath intraoceanic arcs are significantly different than for ophiolites. Unlike Oman, where decompression melting likely resulted in the removal of water, the mantle beneath island arcs is fluxed by H_2O or hydrous melts derived from the subducting slab. In addition, the deformation beneath arcs occurs at higher pressures, and thus the concentration of H_2O in the olivine would be greater (refer to the equation above).

[45] An additional implication for slip on (001)[100], if H_2O induced, is that it may be the dominant slip system in the oceanic asthenosphere at depths below the melting region of mid-oceanic ridges. Estimates of C_{OH} in olivine in the oceanic upper mantle based on electrical conductivity [e.g., *Lizarralde et al.*, 1995; *Hirth et al.*, 2000] or partition coefficients [e.g., *Hirth and Kohlstedt*, 1996] are ~800–3000 H/10^6 Si, high enough to suggest that olivine deformation in the upper oceanic mantle may be dominated by one of the H_2O-induced slip systems. Slip on (001)[100] is more likely than its conjugate (100)[001] system because fast *S* wave polarizations from oceanic plates are consistent with the alignment of [100] axes parallel to the flow direction [*Hiramatsu and Ando*, 1996; *Wolfe and Solomon*, 1998].

5.3. False Arc-Parallel Flow

[46] Fast *S* wave polarizations have been observed parallel to the strike of several active intraoceanic arcs (see

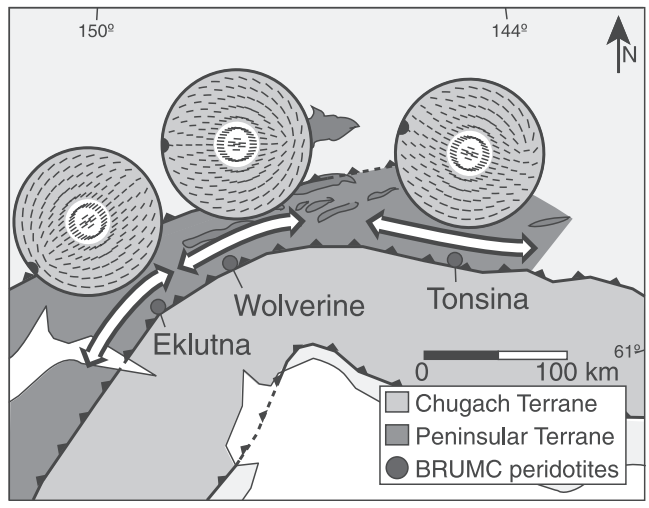

Figure 13. Calculated V_{S_1} polarization planes for bulk Talkeetna arc peridotites. The fast seismic component is subparallel to the mineral lineation (black dot on stereoplot) and inferred strike of the arc over a distance of ~200 km. Steroplots are in map view, white region indicates the shear wave window.

references in section 1). The assumption that the fast polarization contains the olivine [100] maxima and is therefore subparallel to the (subhorizontal) flow direction at high strain leads to the interpretation of arc-parallel mantle flow in these settings. However, arc-parallel flow is not accounted for in most mantle wedge flow models, which assume that flow is dominated by back arc extension [*Fischer and Wiens*, 1996; *Fouch and Fischer*, 1996] or 2-D corner flow induced by the subducting slab [e.g., *McKenzie*, 1979; *Ribe*, 1989; *Fischer et al.*, 2000]. Various scenarios that incorporate arc-normal mantle flow and produce the observed arc-parallel fast polarization planes have been envisioned:

[47] 1. Arc-parallel fast polarizations could be due to the passage of the seismic waves through bodies other than the mantle wedge, such as the subducting slab [*Hiramatsu and Ando*, 1996] or asthenosphere for SKS phases [*Russo and Silver*, 1994]. Subslab anisotropy has been proposed to account for arc-parallel anisotropy measured by SKS waves passing beneath the Nazca plate [*Russo and Silver*, 1994], and beneath the North Island of New Zealand [*Gledhill and Stuart*, 1996].

[48] 2. In addition to the "wet" (100)[001] moderate stress system discussed above, *Jung and Karato* [2001] observed fabrics dominated by slip along (010)[001] at higher stresses. If dominant, this slip system could align olivine fast [100] axes parallel to the arc even though mantle flow is perpendicular to the arc. While this theory merits consideration because the arc mantle may be hydrated, we did not observe fabrics indicative of this slip system.

[49] 3. The presence of melt in aligned fractures or dikes can result in seismic anisotropy [*Kendall*, 1994]. Melt propagating in arc-parallel conduits through the mantle wedge could produce an arc-parallel fast polarization. Although this is likely a significant factor in some arcs, particularly those with back arc extension, the Talkeetna arc provides evidence for arc-parallel flow without such features.

5.4. True Arc-Parallel Flow

[50] LPOs from the Bernard section indicate that the olivine [100] slip direction became aligned to within $\sim 20^\circ$ of the stretching direction. The stretching direction is parallel to the inferred strike of the arc at several locales, suggesting that mantle flow was arc parallel, and supporting the common assumptions made when using seismic anisotropy as a constraint for the kinematics of mantle flow. Given this evidence for arc-parallel flow within a mantle wedge, we reexamine models that incorporate 3-D flow within the mantle wedge.

[51] It is important to clarify that the Talkeetna peridotites represent residual mantle from beneath a Jurassic intraoceanic arc. The high-temperature fabrics within the peridotites likely formed during asthenospheric flow because, unlike continental lithosphere, arcs have relatively simple histories. We expect the Talkeetna arc lithosphere to either have retained fabrics from the spreading center where it formed, or developed due to the flow of the asthenosphere within the mantle wedge beneath the arc. The latter is most likely based on the similar kinematics observed for residual mantle rocks and the ultramafic cumulates above the Moho, and that evidence suggests deformation occurred at asthenospheric temperatures.

[52] First, we address strain in the mantle wedge. Figure 14 illustrates three end-member scenarios for the orientation of the foliation and stretching direction within the arc mantle, and *S* wave polarization orientations for high strain on the (010)[100] and (001)[100] slip systems. Two-dimensional corner flow and any of olivine's high-temperature {0kl}[100] systems align the fast olivine [100] axes parallel to the convergence direction (Figure 14a). Fast polarization planes have been observed subparallel to the convergence direction at many active arcs [see review by *Savage*, 1999], supporting this model for many tectonic settings.

[53] The fast polarization plane has also been measured parallel to many arcs. In this case, it is commonly assumed that arc-parallel flow induces a foliation that is vertical and parallel to the strike of the arc [*Yang et al.*, 1995; *Fouch and Fischer*, 1996]. This foliation orientation results from the assumption that the principal shortening direction, or plate motion, is horizontal and suborthogonal to the arc. If the foliation is vertical and slip occurs on any of the {0kl}[100] systems, the active slip plane is parallel to the vertical foliation and the [100] slip direction is parallel to the trend of the arc, as shown in Figure 14b. There is no evidence for a vertical foliation in the Talkeetna arc peridotites.

[54] A relatively unexplored alternative, indicated by structural analysis of the Bernard Mountain section, is that flow in the mantle wedge is arc parallel, but that the foliation is horizontal (Figure 14c); a similar model for continental lithosphere has been suggested by *Meissner et al.* [2002]. The calculated *S* wave polarization planes for the two possibilities *b* and *c* are indistinguishable. Thus without knowledge of the active olivine slip system(s), *S* wave polarization alone can only be used to assess the extension or flow direction, and cannot be used to determine the orientation of the foliation or flow plane.

[55] Given that arc-parallel flow is a real phenomenon, we illustrate several schematic 3-D flow models to explain arc-parallel flow (Figure 14d) [see also *Wiens and Smith*, 2003]. Perhaps the simplest explanation is homogenous transpression due to oblique convergence. Most plate boundaries have a significant component of arc-parallel plate motion [*Jarrard*, 1986], and numerical modeling indicates that LPOs and seismic anisotropy developed under transpression are consistent with seismic observations at some active arcs [*Tommasi et al.*, 1999]. However, there are also arcs with nearly orthogonal convergence where the fast *S* wave component has been observed parallel to the strike of the arc, such as the eastern Aleutians [*Yang et al.*, 1995] and the Lau back arc [*Smith et al.*, 2001], so oblique convergence alone does not provide the answer. Other factors that may contribute to arc-parallel flow include the rates of convergence and trench migration [*Fouch and Fischer*, 1996; *Buttles and Olson*, 1998], or impediment of the wedge mantle by the slab. *Smith et al.* [2001] proposed that observations of arc-parallel fast components in the Lau basin and Tonga mantle wedges are due to a combination of slab rollback and arc-parallel mantle flow entering from a tear in the Pacific plate. Similarly, complex wedge flow could also result from a nonplanar subducting slab, with arc-parallel flow driven by slab topography.

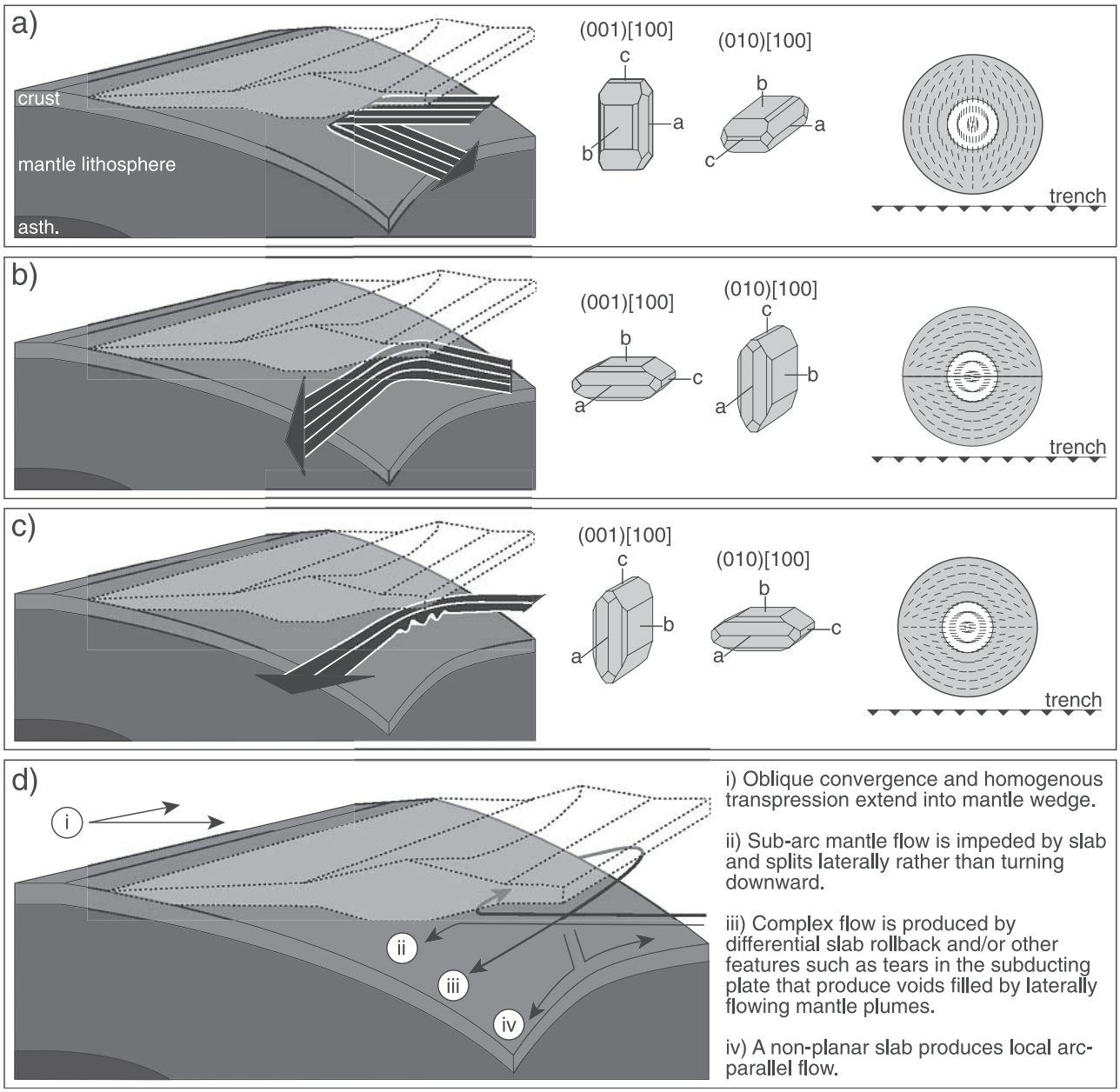

Figure 14. Flow within the subarc asthenospheric mantle. Upper mantle flow indicated by solid arrows, arrows are flat parallel to the foliation plane. The orientation of olivine crystals deformed by slip on (001)[100] and (010)[100] are shown in the same reference frame as the arc, a = [100], b = [010], c = [001]. Plan view stereoplots indicate calculated V_{S_1} polarization planes at high strain. Foliation is indicated by heavy lines, incidence angles outside of the *S* wave window are shaded gray. (a) Two-dimensional corner flow aligns fast olivine [100] axes parallel to plate convergence. (b) Arc-parallel flow in subvertical planes with a vertical foliation, which produces a fast *S* wave polarization plane parallel to the strike of the arc. (c) Arc-parallel flow in subhorizontal planes consistent with the Talkeetna fabrics. The same polarization plane orientations are calculated with a horizontal foliation and slip on (001)[100] as for slip on (010)[100] illustrated in Figure 14b. (d) Models that account for arc-parallel flow within the mantle wedge; arrows are not drawn to imply that each process occurs at a specific depth.

6. Conclusions

6.1. Olivine Deformation

[56] 1. Peridotite fabrics from the mantle of the accreted Talkeetna arc indicate dislocation creep of olivine primarily on the (001)[100] slip system, plus subsidiary slip along the {0kl}[100] and (010)[100] slip systems. These three systems, as well as coarse porphyroclastic textures, indicate deformation at temperatures of ~1000° to >1100°C, consistent with minimum PT constraints of 1.1 GPa and 1025°C from the garnet-gabbro/norites exposed above the Moho at Bernard Mountain. Since the temperature estimates across the Moho are equivalent, we believe that the lithospheric mantle fabrics developed during growth of the arc and in response to asthenospheric flow.

[57] 2. Slip on (001)[100] has only rarely been observed to dominate deformation of peridotites. We suspect that (001)[100] is induced by elevated H_2O activity given the subduction zone setting. In addition, the (001)[100] slip system may be the dominant slip system in the asthenosphere: H_2O concentration estimates in the oceanic upper mantle are high enough for H_2O-induced slip and seismic observations are consistent with alignment of olivine [100] axes parallel to the flow direction.

6.2. Implications for Modern Arcs: Seismic Anisotropy

[58] 1. Slip on (001)[100] with a horizontal foliation and slip on (010)[100] with vertical foliation yield the same calculated *S* wave polarization. This means that the *S* wave anisotropy observed at modern arcs may be due to the (001)[100] slip system active in the Talkeetna arc rather than the commonly assumed (010)[100] slip system, and *S* wave polarization alone cannot be used to infer the orientation of the foliation or flow plane.

[59] 2. *S* wave anisotropy calculations for Talkeetna arc samples, in agreement with calculations and measurements for other natural samples, are significantly greater than measurements at active subduction zones. This discrepancy could be due to variation in the flow direction, or orientation of olivine [100] axes, within the mantle sampled by the *S* waves, indicating complex flow within the mantle wedge. *S* waves passing through the mantle wedge would only need an ~80-km-thick anisotropic layer with Talkeetna-type fabrics to produce the 1-s delay time typical of most subduction-zone measurements.

6.3. Implications for Modern Arcs: Arc-Parallel Flow

[60] 1. In the Talkeetna arc, the stretching direction, the [100] olivine slip direction, and the long axis of the arc are subparallel, indicating that mantle flow was parallel to the arc axis. This alignment of olivine [100] axes produces an *S* wave anisotropy with the fast polarization direction subparallel to the arc. Thus the fast polarization directions observed parallel to some modern arcs now have an exposed geological analog.

[61] 2. Arc-parallel fast polarization directions can be caused by anisotropic peridotites and do not require the presence of fracture zones, fluid-filled pockets, or the high-stress H_2O-induced (010)[001] slip system proposed by *Jung and Karato* [2001].

[62] **Acknowledgments.** Dave Pierce and Scott Sitzman provided crucial technical support with the SEM/EBSD at UCSB. Matt Rioux and Adam Maloof helped with fieldwork. L. M. thanks the Carleton B.A.N.A.L. tectonics workgroup, Dave Root, Emily Walsh, Dave Young, and especially Matt Rioux for helpful discussions at UCSB. This research was funded by NSF grant EAR 9910899. Haemyeong Jung and Alain Vauchez provided very helpful reviews.

References

Avé Lallemant, H. G., Experimental deformation of diopside and websterite, *Tectonophysics*, *48*, 1–27, 1978.

Baker, M. B., T. L. Grove, and R. Price, Primitive basalts and andesites from the Mt. Shasta region, N. California: Products of varying melt fraction and water content, *Contrib. Mineral. Petrol.*, *118*, 111–129, 1994.

Barker, F., and A. Grantz, Talkeetna Formation in the south-eastern Talkeetna Mountains, southern Alaska: An Early Jurassic andesitic island arc, *Geol. Soc. Am. Abstr. Programs*, *14*, 147, 1986.

Barruol, G., G. Helffrich, and A. Vauchez, Shear wave splitting around the northern Atlantic: Frozen Pangaean lithospheric anisotropy?, *Tectonophysics*, *279*, 135–148, 1997.

Barruol, G., A. Souriau, A. Vauchez, J. Diaz, J. Gallart, J. Tubia, and J. Cuevas, Lithospheric anisotropy beneath the Pyrenees from shear wave splitting, *J. Geophys. Res.*, *103*, 30,039–30,053, 1998.

Ben Ismaïl, W., and D. Mainprice, An olivine fabric database: An overview of upper mantle fabrics and seismic anisotropy, *Tectonophysics*, *296*, 145–158, 1998.

Bostock, M. G., and J. F. Cassidy, Variations is SKS splitting across western Canada, *Geophys. Res. Lett.*, *22*(1), 5–8, 1995.

Bouchez, J. L., G. S. Lister, and A. Nicolas, Fabric asymmetry and shear sense in movement zones, *Geol. Rundsch.*, *72*(2), 401–419, 1983.

Burns, L. E., The Border Ranges ultramafic and mafic complex, south central Alaska: Cumulate fractionates of island arc volcanics, *Can. J. Earth Sci.*, *22*, 1029–1038, 1985.

Buttles, J., and P. Olson, A laboratory model of subduction zone anisotropy, *Earth Planet. Sci. Lett.*, *164*, 245–262, 1998.

Bystricky, M., K. Kunze, L. Burlini, and J.-P. Burg, High shear strain of olivine aggregates: Rheological and seismic consequences, *Science*, *290*, 1564–1567, 2000.

Carter, N. L., and H. G Avé Lallemant, High temperature flow of dunite and peridotite, *Geol. Soc. Am. Bull.*, *81*, 2181–2202, 1970.

Ceuleneer, G., A. Nicolas, and F. Boudier, Mantle flow patterns at an oceanic spreading centre: The Oman peridotites record, *Tectonophysics*, *151*, 1–26, 1988.

Debari, S. M., and R. G. Coleman, Examination of the deep levels of an island arc: Evidence from the Tonsina ultramafic-mafic assemblage, Tonsina, Alaska, *J. Geophys. Res.*, *94*, 4373–4391, 1989.

Durham, W. B., and C. Goetze, Plastic flow of oriented single crystals of olivine: 1. Mechanical data, *J. Geophys. Res.*, *82*, 5737–5770, 1977.

Fischer, K. M., and D. A. Wiens, The depth distribution of mantle anisotropy beneath the Tonga subduction zone, *Earth Planet. Sci. Lett.*, *142*, 253–260, 1996.

Fischer, K. M., E. M. Parmentier, A. R. Stine, and E. R. Wolf, Modeling anisotropy and plate-driven flow in the Tonga subduction zone back arc, *J. Geophys. Res.*, *105*, 16,181–16,191, 2000.

Fouch, M. J., and K. M. Fischer, Mantle anisotropy beneath Northwest Pacific subduction zones, *J. Geophys. Res.*, *101*, 15,987–16,002, 1996.

Fouch, M. J., and K. M. Fischer, Shear wave anisotropy in the Mariana subduction zone, *Geophys. Res. Lett.*, *25*(8), 1221–1224, 1998.

Fouch, M. J., K. M. Fischer, E. M. Parmentier, M. E. Wysession, and T. J. Clarke, Shear wave splitting, continental keels, and patterns of mantle flow, *J. Geophys. Res.*, *105*, 6255–6275, 2000.

Frisillo, A. L., and G. R. Barsch, Measurement of single-crystal elastic constants of bronzite as a function of pressure and temperature, *J. Geophys. Res.*, *77*, 6360–6384, 1972.

Gledhill, K., and G. Stuart, Seismic anisotropy in the fore-arc region of the Hikurangi subduction zone, New Zealand, *Phys. Earth Planet. Inter.*, *95*(3–4), 211–225, 1996.

Hess, H. H., Seismic anisotropy of the uppermost mantle under oceans, *Nature*, *203*(4945), 629–630, 1964.

Hiramatsu, Y., and M. Ando, Seismic anisotropy near source region in subduction zones around Japan, *Phys. Earth Planet. Inter.*, *95*(3–4), 237–250, 1996.

Hirth, G., and D. L. Kohlstedt, Water in the oceanic upper mantle: Implications for rheology, melt extraction and the evolution of the lithosphere, *Earth Planet. Sci. Lett.*, *144*, 93–108, 1996.

Hirth, G., and D. L. Kohlstedt, Viscosity of the upper mantle: The Experimentalist's point of view, in *Inside the Subduction Factory, MARGINS Theoretical and Experimental Inst.*, *Earth Sci. Ser.*, vol. II, edited by T. Plank and M. M. Hirschmann, Columbia Univ. Press, New York, in press, 2003.

Hirth, G., R. L. Evans, and A. D. Chave, Comparison of continental and oceanic mantle electrical conductivity: Is the Archean lithosphere dry?, *Geochem. Geophys. Geosyst.*, *1*, Paper number 2000GC000048, 2000.

Jarrard, R. D., Relations among subduction parameters, *Rev. Geophys.*, *24*(2), 217–284, 1986.

Jung, H., and S.-I. Karato, Water-induced fabric transitions in olivine, *Science*, *293*, 1460–1463, 2001.

Kelemen, P. B., J. Rilling, E. M. Parmentier, L. Mehl, and B. R. Hacker, Thermal structure due to solid states flow in the mantle wedge beneath arcs, in *Geophysical Monograph Series*, vol. 138, edited by J. M. Eiler, AGU, Washington, D. C., in press, 2003.

Kendall, J. M., Teleseismic arrivals at a mid-ocean ridge; effects of mantle melt and anisotropy, *Geophys. Res. Lett.*, *21*(4), 301–304, 1994.

Kumazawa, M., The elastic constants of single-crystal orthopyroxene, *J. Geophys. Res.*, *74*, 5973–5980, 1969.

Kumazawa, M., and O. L. Anderson, Elastic moduli, pressure derivatives, and temperature derivatives of single-crystal olivine and single-crystal forsterite, *J. Geophys. Res.*, *74*, 5961–5972, 1969.

Lee, K.-H., Z. Jiang, and S.-I. Karato, A scanning electron microscope study of the effects of dynamic recrystallization on lattice preferred orientation in olivine, *Tectonophysics*, *351*, 331–341, 2002.

Levien, L., D. J. Weidner, and C. T. Prewitt, Elasticity of diopside, *Phys. Chem. Miner.*, *4*, 105–113, 1979.

Lister, G. S., and A. W. Snoke, S-C mylonites, *J. Struct. Geol.*, *6*, 617–638, 1984.

Lizarralde, D., A. Chave, G. Hirth, and A. Schultz, Northeastern Pacific mantle conductivity profile from long-period magnetotelluric sounding using Hawaii-to-California submarine cable data, *J. Geophys. Res.*, *100*, 17,837–17,854, 1995.

Mackwell, S. J., D. L. Kohlstedt, and M. S. Paterson, The role of water in the deformation of olivine single crystals, *J. Geophys. Res.*, *90*, 11,319–11,333, 1985.

Mainprice, D. A., A FORTRAN program to calculate seismic anisotropy from the lattice preferred orientation of minerals, *Comput. Geosci.*, *16*, 385–393, 1990.

Matsui, M., and W. R. Busing, Calculations of the elastic constants and high-pressure properties of diopside, $CaMgSi_2O_6$, *Am. Mineral.*, *69*, 1090–1095, 1984.

McKenzie, D., Finite deformation during fluid flow, *Geophys. J. R. Astron. Soc.*, *58*, 689–715, 1979.

Means, W. D., The concept of steady-state foliation, *Tectonophysics*, *78*, 179–199, 1981.

Meissner, R., W. D. Mooney, and I. Artemieva, Seismic anisotropy and mantle creep in young orogens, *Geophys. J. Int.*, *149*, 1–14, 2002.

Mercier, J.-C. C., Olivine and pyroxenes, in *Preferred Orientation in Deformed Metals and Rocks*: *An Introduction to Modern Texture Analysis*, edited by H.-R. Wenk, pp. 407–430, Academic, San Diego, Calif., 1985.

Mercier, J.-C. C., and A. Nicolas, Textures and fabrics of upper-mantle peridotites as illustrated by xenoliths from basalts, *J. Petrol.*, *16*(2), 454–487, 1975.

Millholland, M. A., C. M. Graubard, J. M. Mattinson, and W. C. McClelland, U-Pb age of zircons from the Talkeetna Formation, Johnson river area, Alaska, *Isochron West*, *50*, 9–11, 1987.

Nicolas, A., Why fast polarization directions of SKS seismic waves are parallel to mountain belts, *Phys. Earth Planet. Inter.*, *78*, 337–342, 1993.

Nicolas, A., and J. P. Poirier, *Crystalline Plasticity and Solid State Flow in Metamorphic Rocks*, 444 pp., John Wiley, Hoboken, N. J., 1976.

Nicolas, A., and A. Prinzhofer, Cumulative or residual origin for the transition zone in ophiolites: Structural evidence, *J. Petrol.*, *24*(2), 188–206, 1983.

Nicolas, A., and J. F. Violette, Mantle flow at oceanic spreading centers: Models derived from ophiolites, *Tectonophysics*, *81*, 319–339, 1982.

Nicolas, A., F. Boudier, and A. M. Boullier, Mechanisms of flow in naturally and experimentally deformed peridotites, *Am. J. Sci.*, *273*, 853–876, 1973.

Nicolas, A., F. Boudier, and J.-L. Bouchez, Interpretation of peridotite structures from ophiolitic and oceanic environments, *Am. J. Sci.*, *280-A*, 192–210, 1980.

Pavlis, T. L., Origin and age of the Border Ranges fault of southern Alaska and its bearing on the late Mesozoic tectonic evolution of Alaska, *Tectonics*, *1*, 343–368, 1982.

Plafker, G., W. J. Nokleberg, and J. S. Lull, Bedrock geology and tectonic evolution of the Wrangellia, Peninsular, and Chugach terranes along the Trans-Alaska Crustal Transect in the Chugach mountains and southern Copper River basin, Alaska, *J. Geophys. Res.*, *94*, 4255–4295, 1989.

Rabinowicz, M., A. Nicolas, and J. L. Vigneresse, A rolling mill effect in asthenosphere beneath oceanic spreading centers, *Earth Planet. Sci. Lett.*, *67*, 97–108, 1984.

Ribe, N., A continuum theory for lattice preferred orientations, *Geophys. J. R. Astron. Soc.*, *97*, 199–207, 1989.

Rioux, M. E., L. Mehl, B. R. Hacker, J. Mattinson, P. B. Gans, and J. L. Wooden, Understanding island arc evolution through U/Pb and $^{40}Ar/^{39}Ar$ geochronology of the Talkeetna Arc, south-central Alaska, *Eos Trans. AGU*, *82*(47), Fall Meet. Suppl., Abstract T41C-0885, 2001.

Russo, R. M., and P. G. Silver, Trench-parallel flow beneath the Nazca plate from seismic anisotropy, *Science*, *263*, 1105–1111, 1994.

Savage, M. K., Seismic anisotropy and mantle deformation; what have we learned from shear wave splitting?, *Rev. Geophys.*, *37*(1), 65–106, 1999.

Silver, P. G., Seismic anisotropy beneath the continents: Probing the depths of geology, *Annu. Rev. Earth Planet. Sci.*, *24*, 385–432, 1996.

Smith, G. P., D. A. Wiens, K. M. Fischer, L. M. Dorman, S. C. Webb, and J. A. Hildebrand, A complex pattern of mantle flow in the Lau Backarc, *Science*, *292*, 713–716, 2001.

Suhr, G., Evaluation of upper mantle microstructures in the Table Mountain massif (Bay of Islands Ophiolite), *J. Struct. Geol.*, *15*, 1273–1292, 1993.

Tödheide, K., Water at high temperatures and pressures, in *Water, a Comprehensive Treatise*, edited by F. Granks, pp. 463–514, Plenum, New York, 1972.

Tommasi, A., B. Tikoff, and A. Vauchez, Upper mantle tectonics: Three-dimensional deformation, olivine crystallographic fabrics and seismic properties, *Earth Planet. Sci. Lett.*, *168*, 173–186, 1999.

Tommasi, A., D. Mainprice, G. Canova, and Y. Chastel, Viscoplastic self-consistent and equilibrium-based modeling of olivine preferred orientations: Implications for the upper mantle seismic anisotropy, *J. Geophys. Res.*, *105*, 7893–7908, 2000.

Van Der Wal, D., R. L. M. Vissers, M. R. Drury, and E. H. Hooderduijn Strating, Oblique fabrics in porphyroclastic Alpine-type peridotites: A shear-sense indicator for upper mantle flow, *J. Struct. Geol.*, *14*, 839–846, 1992.

Wenk, H.-R., and C. N. Tomé, Modeling dynamic recrystallization of olivine aggregates deformed in simple shear, *J. Geophys. Res.*, *104*, 25,513–25,527, 1999.

Wiens, D. A., and G. P. Smith, Seismological constraints on structure and flow patterns within the mantle wedge, in *Geophysical Monograph Series*, vol. 138, edited by J. M. Eiler, AGU, Washington, D. C., in press 2003.

Winkler, G. R., Geologic map and summary geochronology of the anchorage 1°×3° quadrangle, southern Alaska, *U. S. Geol. Surv. Misc. Geol. Invest. Ser. Rep.*, *I-2283*, 1:250,000, 1992.

Winkler, G. R., M. L. Silberman, A. Grantz, R. J. Miller, and E. M. MacKevett Jr., Geologic map and summary geochronology of the Valdez quadrangle, southern Alaska, *U. S. Geol. Surv. Open File Rep.*, *80-892-A*, 1:250,000, 1981.

Wolfe, C. J., and S. C. Solomon, Shear-wave splitting and implications for mantle flow beneath the MELT region of the East Pacific Rise, *Science*, *280*, 1230–1232, 1998.

Yang, X., K. M. Fischer, and G. A. Abers, Seismic anisotropy beneath the Shumagin Islands segment of the Aleutian-Alaska subduction zone, *J. Geophys. Res.*, *100*, 18,165–18,177, 1995.

Zhang, S., and S.-I. Karato, Lattice preferred orientation of olivine aggregates deformed in simple shear, *Nature*, *375*(6534), 774–777, 1995.

Zhang, S., S.-I. Karato, J. Fitz Gerald, U. H. Faul, and Y. Zhou, Simple shear deformation of olivine aggregates, *Tectonophysics*, *316*, 133–152, 2000.

Zhao, Y. H., S. G. Ginsberg, and D. L. Kohlstedt, Solubility of hydrogen in olivine: Effects of temperature and Fe content, *Contrib. Mineral. Petrol.*, in press, 2003.

B. R. Hacker and L. Mehl, Department of Geological Sciences, University of California, Santa Barbara, CA 93106-9630, USA. (hacker@geology.ucsb.edu; mehl@umail.ucsb.edu)

G. Hirth and P. B. Kelemen, Department of Geology and Geophysics, Woods Hole Oceanographic Institution, Woods Hole, MA 02543, USA. (ghirth@whoi.edu; peterk@whoi.edu)